UNIVERSIDAD DE CHILE
FACULTAD DE CIENCIAS FÍSICAS Y MATEMÁTICAS
DEPARTAMENTO DE INGENIERÍA ELÉCTRICA

AN IMPROVED PROGNOSIS STRATEGY WITH TEMPERATURE DEPENDENT STATE-SPACE MODEL FOR THE ANALYSIS OF THE STATE-OF-HEALTH AND STATE-OF-CHARGE IN LITHIUM-ION BATTERIES.

TESIS PARA OPTAR AL GRADO DE MAGÍSTER EN CIENCIAS DE LA INGENIERÍA MENCIÓN ELÉCTRICA

MEMORIA PARA OPTAR AL TÍTULO DE INGENIERO CIVIL ELÉCTRICO

DANIEL ARTURO POLA CONTRERAS

PROFESOR GUÍA:
MARCOS ORCHARD CONCHA

MIEMBROS DE LA COMISIÓN:
JORGE SILVA SÁNCHEZ
JUAN YUZ EISSMANN

SANTIAGO DE CHILE
AGOSTO 2014

Resumen de la Memoria para Optar al Título de
Ingeniero Civil Eléctrico y Grado de Magíster
en Ciencias de la Ingeniería Mención Eléctrica
Por: Daniel Arturo Pola Contreras
Fecha: Agosto 2014
Profesor Guía: Marcos Orchard Concha

AN IMPROVED PROGNOSIS STRATEGY WITH TEMPERATURE DEPENDENT STATE-SPACE MODEL FOR THE ANALYSIS OF THE STATE-OF-HEALTH AND STATE-OF-CHARGE IN LITHIUM-ION BATTERIES.

Actualmente existe una gran cantidad de equipos y dispositivos que utilizan baterías como su fuente primaria o secundaria de energía. Para estos sistemas es crítico contar con información del desempeño de sus baterías, dado que este conocimiento puede ayudar a tomar decisiones apropiadas y asegurar autonomía en el tiempo. Dos importantes variables que deben ser monitoreadas son el "Estado-de-Salud" (SOH, del inglés *State-of-Health*) y el "Estado-de-Carga" (SOC, del inglés *State-of-Charge*). Este trabajo se enfoca en generar esquemas de pronóstico para ambas variables, donde se tome en cuenta la temperatura de operación.

Con este propósito, se diseñaron y realizaron un conjunto de pruebas de laboratorio con celdas de Ion-Litio donde se caracterizó el impacto de la temperatura en factores tales como la energía entregada en un ciclo, la impedancia interna, o tendencia de degradación. A partir de estos datos, y esquemas existentes en la literatura, se proponen modelos empíricos para la degradación y para la descarga de una batería mediante una representación de espacio-estados, definiendo directamente un estado como el SOH y el SOC respectivamente. Las estimaciones y predicciones a largo plazo se efectúan bajo un enfoque Bayesiano, basado en el filtro de partículas. Además, se propone la implementación de lazos de control externos para corregir condiciones iniciales erróneas de los estados, y un módulo de detección de *outliers* para trabajar con datos perdidos o inválidos.

La validación de estos esquemas se realiza con datos generados en laboratorio, además de datos de degradación publicados por NASA Ames Prognostic Center of Excellence. El esquema propuesto para el SOH es capaz de incorporar explícitamente el efecto de la temperatura de operación (bajo el concepto de "Capacidad Usable"), y estimar y pronosticar el SOH a una temperatura de referencia. Por otro lado, el esquema para el SOC fue validado incluyendo una mejor representación de la fenomenología del proceso de descarga comparada a la existente, y se deja una propuesta de cómo incluir el efecto de la temperatura en el modelo.

La implementación de estos esquemas de pronóstico permite la incorporación de la temperatura de operación, que a pesar de su gran influencia en el comportamiento de las baterías es considerada constante en muchos casos presentes en la literatura; además de incluir algunas mejoras prácticas en los algoritmos de estimación. Las propuestas de este trabajo dejan las bases para avanzar en la incorporación de otros fenómenos importantes como la profundidad de descarga, o la magnitud de la corriente de descarga.

Summary

Batteries can be found as primary or secondary energy sources in numerous pieces of equipment and devices. For these systems it is critical to gather information about the battery performance, since this knowledge could help to take appropriate actions and ensure autonomy throughout time. Two important variables that must be monitored are the "State-of-Health" and the "State-of-Charge". This work focuses on formulating prognosis schemes for both variables, explicitly including the temperature of operation within the structure of the predictive model.

A set of laboratory experiments with Lithium-Ion cells were designed and carried out, where the temperature impact on factors such as the energy delivered in a cycle, the internal impedance or the degradation trends was characterized. Considering the collected data sets and the schemes available in the literature, a state-space representation of empirical models for degradation and the discharge process of a battery is proposed; defining directly one state as the SOH and SOC respectively. The estimates and long-term predictions are generated using Bayesian approaches, specifically a particle filter algorithm. Furthermore, the implementation of outer-feedback correction loops to correct erroneous state initializations and a detection module to isolate artifacts created by lost data or outliers is proposed.

The validation of these schemes is made with laboratory-generated data, and public degradation data provided by NASA Ames Prognostic Center of Excellence. The proposed SOH model is able to incorporate explicitly the impact of the temperature of operation (with the concept of "Usable Capacity"), and estimate and predict the SOH at a reference temperature. The SOC prognosis scheme is validated including an improved representation of the phenomenology of the discharge process compared to those found in the literature. Finally, a proposal to include the effect of the internal temperature in the model is discussed.

The implementation of these prognosis schemes allows the incorporation of the temperature of operation, a variable that has been considered constant in some previous works despite of its impact in the performance of the battery; in addition to the inclusion of practical improvements to the algorithms. The propositions introduced in this work set the basis to advance in the incorporation of other important phenomena as the depth of discharge, or the magnitude of the discharge current.

Dedicado a mi familia.

Acknowledgements

Este trabajo de magíster fue parcialmente financiado por el proyecto FONDECYT 1110070 durante el segundo semestre de 2012, y a partir de marzo de 2013 por la beca de Magíster Nacional Complementaria del PFCHA de CONICYT folio 221320011 junto con la Facultad de Ciencias Físicas y Matemáticas de la Universidad de Chile.

Quiero partir agradeciendo a mi profesor guía Marcos Orchard, excelente profesor, docente, y persona. Sin duda aprendí mucho al haber tenido la oportunidad de ser tesista, y no solo de esquemas Bayesianos. También a los profesores Jorge Silva y Juan Yuz que me ayudaron a culminar este trabajo de tesis. A los profesores Marcos Díaz y Roberto Rondanelli con quienes trabajé durante un par de semestres en la radiosonda. Además a los profesores Doris Sáez y Guillermo González de quienes fui ayudante en varias ocasiones. Por supuesto también a compañeros del Laboratorio de Control Avanzado con quiénes trabajé y compartí durante el último tiempo en la U: Benja, Cato, Enrique, Aramis, Francisco, David, Jorge, Marco y Pablo; y también a todos con los que compartí labores de ayudante en Laboratorio de Automática durante los (varios) semestres que estuve. Y nuevamente a los profesores Marcos y Doris por haberme presentado la oportunidad de ir a hacer una pasantía a la Universidad de Waterloo en Canadá (y poder conocer Waterloo, Toronto, Niagara Falls y Montreal).

Hay muchos factores que influyen en la formación de una persona, y uno realmente importante son los amigos. A ustedes no puedo dejar de agradecer toda la buena onda y los buenos ratos, y por haber hecho más grato todo este proceso. A mis amigos eléctricos, y en su mayoría miembros del glorioso Divino Circuito F.C. Club Social y Deportivo: Karel (mención honrosa por la ayuda para mejorar el inglés de este documento), Hugo, Tomás, Piña, Pancho, Pato, Tati, Richi R., Fallo, Wlady, Felipe, Ángela. También a mis amigos de plan común, sobre todo por todas esas horas jugando taca-taca: Javier, Huepe, Diego, Miño, Carlos, Juan, Quirogo, Vicho, Vale, Richi M., etc! Y por supuesto a la manga de ... amigos del colegio y la vida, Franco, Chico, Negro, Hugo, Coomer, Álvaro, Kata, Ale, entre otros.

Finalmente me dirijo a mi familia, quienes estuvieron para aguantarme durante todo el extenso periodo de estudio desde que me mandaron contra mi voluntad al segundo día de clases en prekinder. No puedo no agradecer por cosas como siempre tenerme una rica comida cuando llegaba muerto de hambre después de la U, o el "radiotaxi" esperándome para llevarme a los controles de primer año los sábados a las 8:00 am. Y principalmente la ayuda, apoyo y comprensión para poder sacar esta tarea adelante. ¿Es todo lo que tengo que agradecerles? Ciertamente no, me da para muchísimo más que un simple párrafo, solo quiero que a quien sea que llegue a leer hasta aquí le quede medianamente claro lo fundamental que han sido.

Table of Contents

List of Tables

List of Figures

Chapter 1

Introduction

Energy Storage Devices (ESD), and in particular rechargeable batteries, can be found in a diverse amount of communication, mobile or transport equipments, being either the principal or secondary energy source. Smartphones, tablets, personal computers, digital cameras, satellite phones, hybrid and electric vehicles, satellites, intermittent generators (wind turbines, photovoltaic cells) or micro-grids are examples of applications where batteries are of paramount importance. As a consequence, ESD are a fundamental part of the system design, and may represent a constrain in their operation due to non-satisfied power or energy requirements. This rises the necessity to gather information about the actual state of the ESD, and to make long-term predictions of their performance.

ESD monitoring acquires a great importance for the adequate performance of the devices, being covered by the "Battery Management Systems" (BMS). These systems are mainly aimed at tasks such as: (i) providing real-time information, (ii) reducing battery charging times, (iii) maximizing the amount of operating cycles, (iv) maximizing the usage time associated to the discharge cycle, (v) maintaining the operation of all cells within their rated limits, and (vi) compensating for cell imbalance, among others [1]. To accomplish these tasks, BMS have to consider information about the "State-of-Health" (SOH) and the "State-of-Charge" (SOC). In broad terms, the SOH provides information about how much the ESD has aged over time and by usage conditions, while the SOC provides information of how much energy can be delivered by the ESD before it has to be charged. Both variables cannot be measured or obtained directly from other measurements, and both depend on operational and ambient factors. They have to be estimated from other observed variables as the voltage in terminals, current drained from the ESD, or its temperature.

Battery performance is strongly determined by characteristics such as the current discharge rate, depth of discharge, or the internal temperature. These characteristics are also important for the aging process that affects the battery, and for operational and safety conditions. Given the complexity of the monitoring problem, the estimation of the SOH and SOC has been studied using diverse approaches (neural networks, fuzzy logic, Bayesian filter) and models (electrochemical, circuit-based, empirical). Bayesian tools have been studied to

estimate and generate long-term predictions of both variables, but with some simplifications such as the consideration of constant operating temperature. This operational factor affects directly the chemical reaction rate and the internal impedance of the battery [2], [3], resulting in a modification of the amount of energy that it can store and deliver in a cycle, and the aging process that affects the battery. By this reason, it is important to include it in any SOH/SOC estimation and prognosis scheme.

The general objective of this work is to study and explicitly characterize the impact caused by the operating temperature profile on the performance and operation of SOH/SOC estimation and prognosis schemes, with special emphasis on changes in capacity, internal impedance, and degradation of Lithium-Ion batteries.

The specific objectives are:

- Generate a methodology and a set of experiments to collect data of temperature-dependent capacity, internal impedance, and battery degradation; and generate adequate experiments to study the evolution in time of Li-Ion battery SOC.

- Include explicitly the temperature as an input variable on a SOH prognosis scheme.

- Improve an energy-oriented SOC prognosis scheme, and make a proposal to include the internal temperature.

Chapter 2

Theoretical Framework

The importance of the information provided by the "State-of-Charge" (SOC) and "State-of-Health" (SOH) has been previously mentioned. Although a more precise definition of these parameters require a throughout understanding of electro-chemical aspects in Lithium-Ion (Li-Ion) battery cells, it sufficcess to say that they provide information about the autonomy of the system in use and the remaining useful life of the battery, respectively. To study the problem of estimation and prognosis of battery SOC and SOH, it is first necessary to study a brief introduction to the Li-Ion batteries, their operation and behavior, in addition to concepts related to battery monitoring. It is also needed to introduce the mathematical methods that are used in this work to implement the SOC and SOH prognosis frameworks.

In this regard, the structure of this chapter is as follows. Section 2.1 presents the basic concepts about batteries, their aging mechanisms and some definitions for battery monitoring. Section 2.2 shows a state-of-the-art of the problem of SOC and SOH estimation and prognosis. Section 2.3 focuses on the Bayesian inference problem and sequential Monte Carlo methods for estimation and long-term predictions.

2.1 Lithium-Ion Batteries: Basic Concepts

A battery is an Energy Storage Device (ESD) that transforms chemical energy stored in the active material into electrical energy through redox reaction. A cell is the basic electrochemical unit with a fixed voltage depending on its chemistry, while a battery is a group of cells connected in series, parallel, or a combination of them [4]. Cells, and also batteries, can be separated between primary and secondary type. Primary type are those that are designed to be discharged only once, and secondary type are those that can be charged and discharged many times by their capability of being electrically recharged after a discharge process. Secondary or rechargeable batteries are also called accumulators.

The principal components of batteries are the anode (negative electrode), the cathode (positive electrode), the electrolyte and the separator. In the course of a discharge process, the anode provides electrons to the external circuit being oxidized during the electrochemical reaction. On the other side, the cathode accepts electrons from the external circuit during the discharge, being reduced. The electrolyte is the medium that allows the transport of ions between the anode and cathode, and is typically a liquid or solid with dissolved salts to impart ionic conductivity [4]. The separator is a porous membrane placed between electrodes of opposite polarity, permeable to ionic flow. It protects the battery for short-circuiting and thermal runaway (positive feedback of self heating due to high temperature of operation) [5].

There are different types of batteries including Lead-Acid, Niquel-Metal and lithium-based batteries. Secondary Lithium-Ion (Li-Ion) cells have high voltage ($4[V]$), high specific capacity ($3,86[Ah \cdot g^{-1}]$) and high energy density ($150[Wh \cdot kg^{-1}]$), present no memory effect, have a low self-discharge rate, and permit many charge discharge cycles [6], [7], [8]. Figure 2.1 compares specific power and specific energy for different eletrochemical batteries.

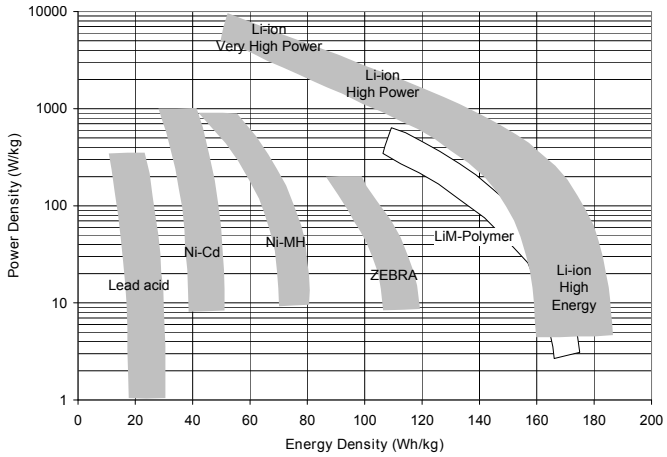

Figure 2.1: Ragone diagram of the main electrochemical devices (adapted from [9]).

In [10] it is exposed that in the most common structure of Li-Ion batteries, the cathode is formed by a lithium metal oxide (e.g., $LiMO_2$), the anode is a graphit anode (e.g., mesocarbon or microbeads), and the electrotyle consists of a solution of a lithium salt (e.g., $LiPF_6$) in a mixed organic solvent embedded in a separator felt. Figure 2.2.a represents the described configuration. An example of the reversible processes involving the extraction and insertion of lithium ions between the electrodes is given in Equation (2.1) for the positive electrode and Equation (2.2) for the negative electrode [7]. Reactions from left to right of the equations corresponds to discharge process and from right to left to charge process.

$$Li_{1-x}MO_2 + x \cdot Li^+ + x \cdot e^- \underset{charge}{\overset{discharge}{\rightleftharpoons}} LiMO_2 \tag{2.1}$$

$$Li_xC_6 \underset{charge}{\overset{discharge}{\rightleftharpoons}} C_6 + x \cdot Li^+ + x \cdot e^- \tag{2.2}$$

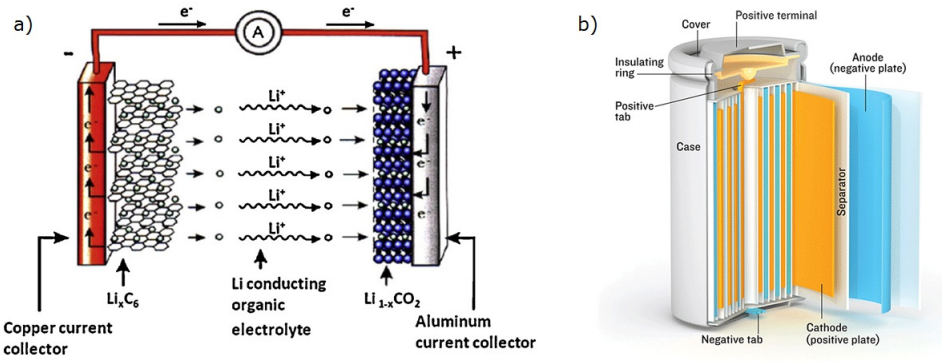

Figure 2.2: Illustriation of a Li-Ion battery, (a) electrochemical scheme of the discharge process [10], and (b) components and configuration of a cylindrical Li-Ion battery [11].

2.1.1 Battery Aging

The concept of aging is related to the finite life of a battery, typically associated with the reduction of energy delivered by the ESD or the growth of its internal impedance. Aging is usually divided from two origins: calendar aging, that is related to the effects of the battery storage; and cycle aging, corresponding to the impact of battery usage over charge and discharge processes.

Many researchers have studied the aging mechanisms in Li-Ion batteries from an electrochemical point of view, separating the aging effects on the anode from aging effects on the cathode, because both electrodes presents different degradation mechanisms. Throughout the remainder of this section, corresponding to the aging mechanisms in the electrodes, the information is obtained from the extensive work done by Vetter *et al.* [12] and Barre *et al.* [13] of aging mechanisms, and for further study is highly recommended to study their publications and their references for each topic.

Anode:

The principal aging factor on a typical graphite anode corresponds to changes at the electrode-electrolyte interface, where a solid interface is developed throughout time. The latter interface is called Solid Electrolyte Interface (SEI). SEI is naturally created at the first charge, and keeps growing during cycling and storage inducing loss of continuous lithium ions and electrolyte decomposition. This interface protects the anode from possible corrosions and the electrolyte from reductions, which provides a guarantee of security. However, the SEI is not stable as Li-Ion battery operates outside the tension stability range of the electrolyte.

The aforementioned SEI layer is permeable to charged elements including lithium ions, or neutral elements (solvent). The solvent interacts with the graphite exfoliation and creates gas that can crack the SEI and therefore allow its expansion. Researchers exposed that the gas formation is low and seems to happen only during storage periods and with high voltages. Figure 2.3 illustrates the evolution of the SEI.
There is a loss of active surface over time with leads to an increase in the electrode impedance,

produced by either storage and utilization of the battery. A high potential difference between electrode interfaces and electrolyte may accelerate these phenomena. In addition, there are other factors that can accelerate the aging process, being temperature one of paramount importance. On the one hand, if the cell undergoes high temperatures the SEI may dissolve and create lithium salts less permeable to the lithium ions, increasing the anode impedance. On the other hand, low temperatures lead to a decrease of the diffusion of lithium within the SEI and graphite, which can overlay the electrode with lithium plating.

The formation and growth of the SEI leads to gradual contact loss within the composite anode, and thus, increases the impedance at the anode. In parallel to SEI growth, corrosion of lithium in the active carbon takes place, leading to self-discharge and capacity fade due to loss of mobile lithium.

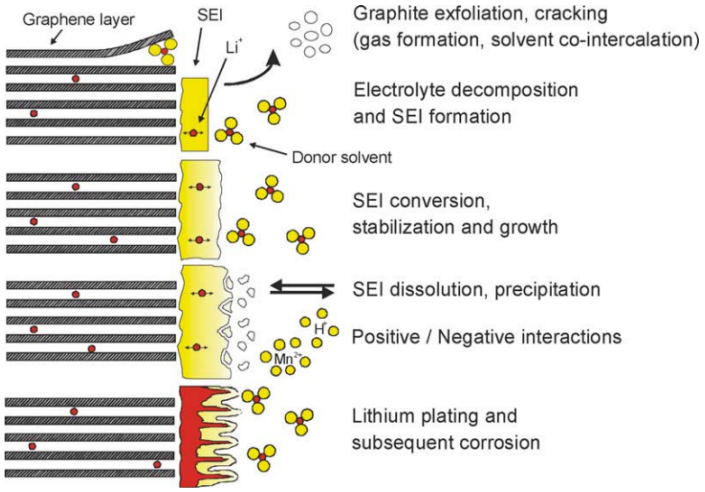

Figure 2.3: Changes at the anode/electrolyte interface [12].

Cathode:

The principal consequences on an aged cathode are electrolyte degradation, electrolyte oxidation, SEI formation, and interaction between the positive electrode element dissolved within the electrolyte and the negative electrode [13]. These effects are not independent and interactions differs with the electrode material. Observations show that there are no changes in the cathode morphology for different types of battery utilization. This leads to the primordial importance of the anode in battery aging.

Consequences of Battery aging:

The performance loss associated with battery aging can be originated from mechanical or chemical mechanisms. The principal consequences related to lithium-ion batteries aging are [13]:

- Loss of cyclable lithium that increases cell imbalance, at either the anode or cathode.
- Loss of electrode active material.
- Increase of cell impedance.

Loss of both cyclable lithium and active material leads to capacity fade. Increase of impedance implies loss of autonomy and maximum power available.

Aging effects associated to the storage time, as self-discharge or impedance rise, will affect the calendar life of the battery, whereas the cycle life is affected by them and also aging effects that occur during usage, as mechanical degradation or lithium metal plating [26].

2.1.2 Important Concepts Related to Battery Monitoring

This section provides some definitions for important concepts related to battery monitoring.

a) Depth-of-Discharge (DOD): The DOD represents, in percentage, how much a battery was discharged compared to the fully charged state (100%). For the case of Li-Ion batteries, the aging mechanisms depends on the DOD value, presenting an exponential relation between lifetime cycles and DOD. Deeper discharges reduce the number of cycles yielded by a battery [14], as can be seen in Figure 2.4.

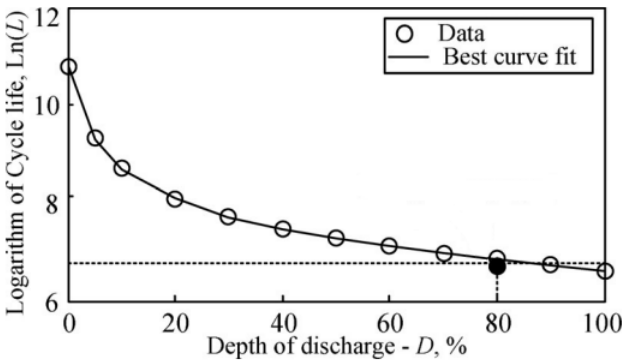

Figure 2.4: Lithium-ion cycle life dependence on DOD (Adapted from [14]).

b) C-rate: The charge or discharge current $I[A]$ of an ESD can be expressed in terms of its rated capacity $C[Ah]$[†]. The C-rate corresponds to a multiplier of the rated capacity that satisfies $I = m \cdot C$. This parameter is usually expressed as a factor multiplied by C and is dimensionless. For example, consider a battery with $C = 1,5[Ah]$ and a discharge current $I = 0,5[A]$, then the C-rate is $C/3$, but if the discharge current were $I = 3[A]$, the C-rate would be $2C$.

c) Capacity and Power Fade: These concepts corresponds to gradual loss of maximum capacity and power of a second type battery respectively.

d) Self-Discharge: Is the phenomenon of reduction of stored energy of an ESD due to internal chemical action.

[†] $1[Ah]$ = 1 Ampere-hour = $3600[A \cdot sec]$

e) State-of-Charge (SOC): The SOC provides an indicator of the system autonomy that directly depends on the remaining energy of a battery in relation to its energy when fully charged. Some approaches considers the SOC as a function of the remaining capacity instead of energy.

For the same temperature, variations on the SOC affects the calendar aging of a battery in a distinct form. For elevated SOC levels, batteries presents higher degradations during storage that can be explained by the great potential disequilibrium on the electrode/electrolyte interface [13].

f) State-of-Health (SOH): The SOH is a manner to relate how much a battery has degraded in comparison to its nominal values, corresponding to an indicator of battery aging. It is typically characterized by one or more of the following: available capacity, internal resistance/impedance, capacity fade, power fade or self-discharge rate. Also, SOH has been studied from charging processes considering the evolution of constant current charge time (CCCT) and constant voltage charge time (CVCT) [15]. Capacity and power fading are originated from various processes and their interaction, which cannot be studied independently and occur at similar timescales.

g) End-of-Discharge (EOD): Corresponds to the time instant when the battery is discharged. Tipically, a battery is considered discharged when it reaches a lower threshold voltage.

h) Charging Constant Current-Constant Voltage (CC-CV) Protocol: In the CC-CV charging protocol [16], a battery is charged with a constant current until the voltage reaches a pre-determined value, followed by a constant voltage until the current drops to a lower limit.

2.1.3 Temperature Impact on Lithium-Ion Batteries Performance

There are many important factors that affect the behavior and performance of Li-Ion cells. These include the DOD, discharge C-rate, charging regimen, and cell temperature, among others [6], [17]. Temperature not only has a strong influence at the performance of charging and discharging processes, but also on cell aging, as discussed in Section 2.1.1. For example, a high temperature will affect the charge and discharge efficiency; however, this high temperature may imply a decrement of the battery lifetime [18].

Li-Ion batteries present an ideal working temperature range in which the operation of the cell is guaranteed. Figure 2.5 shows the effect of ambient temperature on the cycle life of the Li-Ion battery. Outside of the optimal range, the capacity decay is different for high and low temperature, as the aging mechanisms are distinct.

As high rate discharges produces a significant temperature rise, cooling the battery may be necessary to avoid an accelerated aging. Figure 2.6 shows the difference of the cell surface temperature at various discharge rates comparing a normal convection with a forced con-

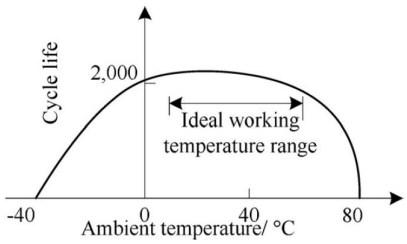

Figure 2.5: Effect of ambient temperature on the cycle life of the Li-Ion battery [14].

vection corresponding to an airflow of 35 m/s [2]. The importance of temperature impact on the performance of lithium-based batteries has been taken in count in the industry. For example, in the commercial electrical vehicle Nissan Leaf^{TM} the temperature of the battery pack is controlled by adjustment of the battery's internal resistance [19], to keep the pack working between some desirable operation range.

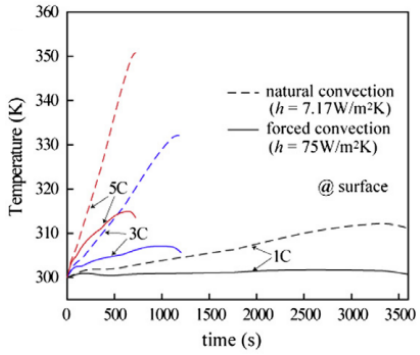

Figure 2.6: Surface temperature profiles under different convection conditions (Adapted From [2]).

Operation temperature affects the performance and the degradation mechanism of a battery. The reaction rate of a battery is described by the Arrhenius equation (2.3) where Φ corresponds to the battery chemical reaction rate; $E_a(\Phi)$ is the activation energy and its magnitude determines the sensitivity of Φ to temperature; R is the gas constant and T the temperature. The subscript ref indicates the values at a reference temperature:

$$\Phi = \Phi_{ref} exp\left(\frac{E_a(\Phi)}{R}\left(\frac{1}{T_{ref}} - \frac{1}{T}\right)\right). \tag{2.3}$$

High temperatures decrease the activation energy for the chemical reaction and more intercalation and deintercalation can take place in the cell; also, the cell voltage is higher and lithium ions can diffuse faster. These effects increase the power capability and the cell can be discharged deeper and deliver more energy [20]. On the other hand, at low temperatures the intercalation and deintercalation at the electrodes require more energy, resulting in less lithium ions involved in the active cell process and also in a lower cell voltage. The lithium ion diffusion will be slower. These effects leads to a temporary loss of both capacity and power [20]. These concepts can be seen in the discharge temperature characteristics curves that can be found in batteries datasheet, as the presented in Figure 2.7.

Excluding the aging associated to battery cycling, the effects recently mentioned are temporary. When the battery is used at nominal temperature after being used at high or low temperature, the capacity and power are restored.

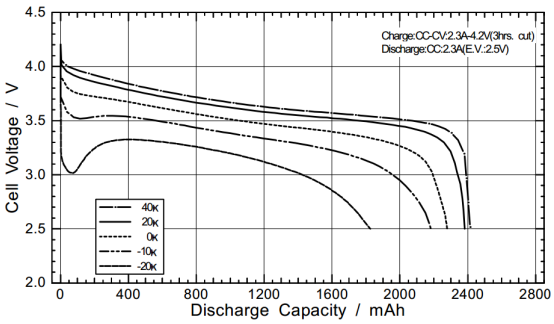

Figure 2.7: SANYO Lithium-Ion UR18650F Cell discharge curves in function of temperature [21].

Due to the variations at the cells produced by different operation temperatures, the internal impedance also presents changes. Figure 2.8 shows a Nyquist plot of the Electro Impedance Spectrogram test made at different temperatures with a SOC of 50%. As can be seen, the impedance is reduced when the temperature is increased, and can be explained by the relation of the chemical reaction rate dependence on temperature.

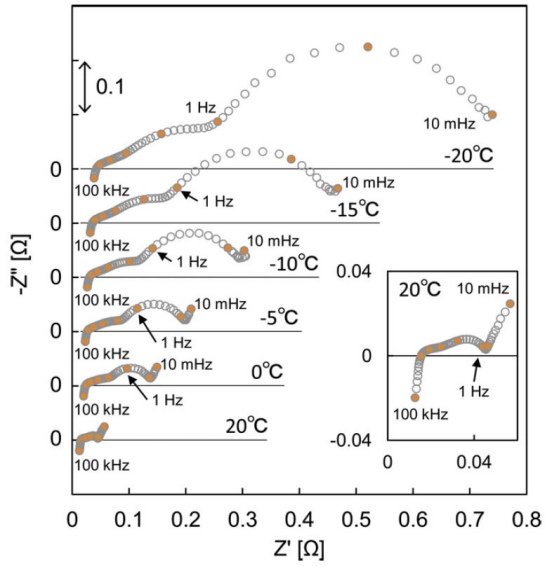

Figure 2.8: Nyquist plots for a Lithium-Ion battery at different temperatures. Each parallel line shows 0[Ω] of Z" at each temperature [3].

2.1.4 Li-Ion Battery Degradation Trends for Different Conditions of Operation

The cycle life of a battery is affected by operating conditions during charge and discharge procedures. In [22], authors studied the effect of various cycling regimes on the aging of 900 [mAh] prismatic Li-Ion cells at ambient temperature. On the one hand, Figure 2.9.a shows the effects of variations at the CV value for a CC-CV charging, with CC of 1C. On the other hand, Figure 2.9.b shows the effects of the variations at the CC value, with CV of 4.2[V]. For both test, cells where discharged at 1C until a cut-off voltage of 2.75[V].

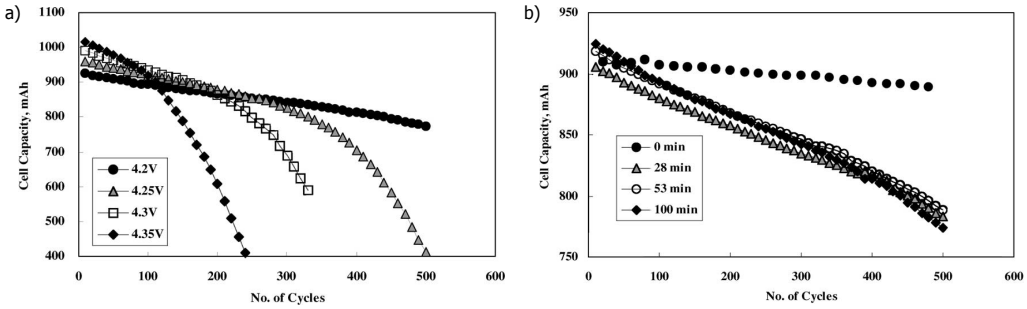

Figure 2.9: (a) Effect of CV charge voltage on cycle performance. (b) Effect of charge rate on cycle performance. (Adapted from [22]).

The effect of the discharge C-rate is presented in Figure 2.10.a, where the battery is charged with CC of 1C, CV of 4.2[V], current cut-off limit of 90[mA], and discharged until the minimum voltage of 2.75[V]. Another test was implemented to examine the effect of the DOD and is shown in Figure 2.10.b, where the discharge was cut-off at various voltages within 2.75[V] and 3.55[V], after fully charging the cell at 1C rate.

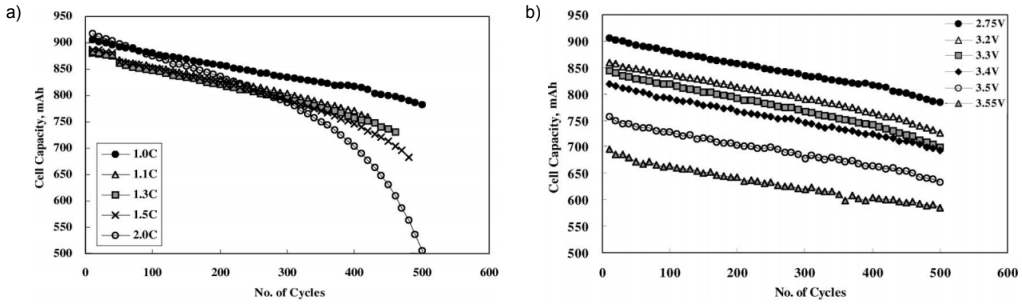

Figure 2.10: (a) Effect of CV charge voltage on cycle performance. (b) Effect of charge rate on cycle performance. (Adapted from [22]).

Their results show the importance of the battery charge procedures that are implemented, on its life-cycle, in addition to a strong dependence on the current discharge rate at ambient temperature. For the studied cut-off voltage range, the degradation trends were similar; however, the impact of cut-off voltages under 2.75[V] (related to high DOD) were not examined.

Temperature has an important role at battery aging, particularly if the operating range is above 55^oC as can be seen in the Figure 2.11, that presents the capacity fade of Sony 18650 cells (1800[mAh], 3.7[V]) cycled at: room temperature (RT), 45^oC, 50^oC and 55^oC.

Batteries were discharged with a constant current of $1[A]$ until a cut-off voltage of $2[V]$. The cells presented a similar variation in capacity loss for the first cycles, but then the cells cycled at 50^oC and 55^oC degraded faster than the other two.

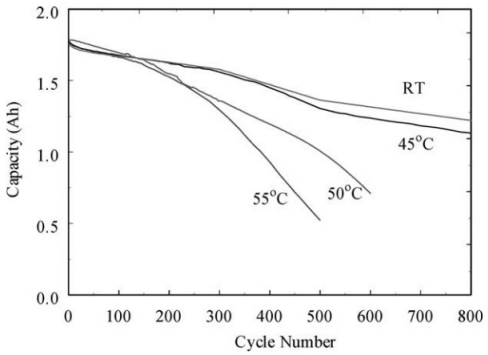

Figure 2.11: Discharge capacity of Sony 18650 cells cycled at different high temperatures [23].

Even though a set of similar cells are cycled with the same conditions, they can degrade in a different manner. Figure 2.12 [24] presents the degradation of 20 cells cycled 800 times with the same conditions. It is clear that below 80% of capacity loss, some cells started to degrade faster than others.

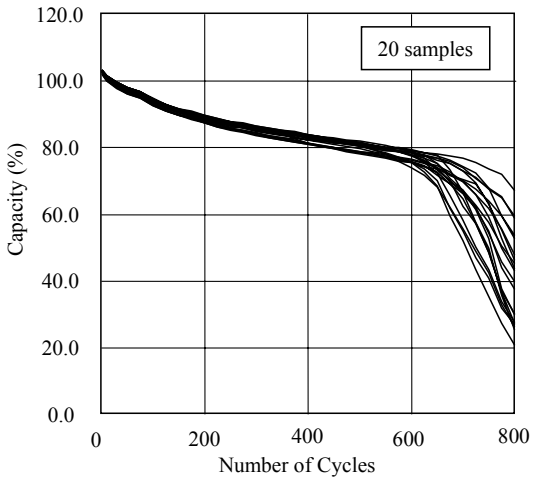

Figure 2.12: Degradation of 20 similar cells under the same operational conditions [24].

Providing this evidence, the internal temperature of a battery affects its aging and also its performance in every cycle. This work focuses on the development of SOH and SOC estimation and prognosis frameworks considering models for battery degradation and battery discharge that includes the impact of the temperature of operation.

2.2 State-of-Charge and State-of-Health Estimation and Prognosis for Energy Storage Devices

An important function of a Battery Management System (BMS) is to provide information about the State of Charge, State of Health and Remaining Useful Life, besides other important tasks such as keeping the balance between cells or compensating for any imbalances in cell parameters within the battery pack [1]. On the one hand, the SOC is used to quantify the autonomy of the system under assumptions of future battery usage. On the other hand, knowledge about the SOH is necessary to determine what kind of degradation process is affecting the ESD and how many cycles can be supported by it before is degraded. Such information could help to decide when to replace a cell or battery pack.

Various methods have been developed to estimate both the SOC and SOH, using different kind of models; including analytical, empirical, electrochemical or probabilistic. The following sections will describe the state-of-the-art for the problems of SOC/SOH estimation and prognosis separately.

2.2.1 State-of-Charge Estimation and Prognosis

The estimation of the SOC of an ESD is not an easy task, mainly because this quantity cannot be measured directly and must be inferred from the observation of other variables as the battery terminals voltage, current, temperature, SOH or self-discharge phenomena [1], [25]. Usually, simple models neglect the dependence of temperature on the battery performance assuming an invariant temperature value (tipically 23^oC). It is important to consider this dependence for the implementation of SOC estimators in any device that requires an accurate characterization of this parameter in real-time. Changes on the battery's temperature or ambient temperature imply changes of important model parameters like the battery energy in a fully charged state, or the internal impedance.

The most popular techniques used to estimate the SOC are Coulomb counting and the relation between open circuit voltage (OCV) and SOC. The Coulomb counting method approximates the charge inside a battery by integrating the current of a charge/discharge process. This method presents the advantage of an easy implementation and can be used for on-line applications. However, it requires accurate current measurements, is affected by parasitic currents, is susceptible to systematic errors, does not take into account current loss by internal resistance, among others [1], [26]. The advantage of the OCV method is that it presents a direct relation between the OCV measurements and SOC, but requires rest periods of the battery, limiting its use for on-line applications [1], [26], [27].

The utilization of complex electrochemical models for the battery has been only suitable for off-line studies, mainly because they require extremely accurate measurements, count with many variables in the model, and have to be adjusted carefully when a different battery

is studied [1], [26]. However, these models are highly accurate as they include dependence of parameters on diverse variables based on the electrochemical behavior of the battery, considering, for example, the operation temperature or the magnitude of the current flowing throw the battery.

In order to achieve the task of SOC estimation and prognosis, current research efforts have focused on approaches that are mostly based on empirical models that incorporate only critical phenomenological aspects of the process, as the relationship between currents, voltages and temperatures of Li-Ion cells. Among these methods, it is worth to mention those that are based on fuzzy logic, neural networks, or Bayesian approaches.
A widely used option for the empirical models is to consider an electrical equivalent circuit for the battery, to represent the chemical behavior of the ESD. The most common topology for Li-Ion battery equivalent circuit consist of a resistance (representing the electrolyte resistance) in series with one or more RC branch to include a proper characterization of transient phenomena (dual layer capacitance, charge transfer resistance or concentration polarization effect) [28]. Some of these equivalent circuits include explicitly the temperature effect on the value of the parameters [29], [30], but other neglect that dependence [1], [28], [31]. However, some models based on equivalent circuit with invariant parameters consider a correction potential to compensate variations of equilibrium potential induced by the temperature [28], [31].

Fuzzy logic models have been used for the SOC estimation by the identification of equivalent circuit for the battery from Electrochemical Impedance Spectroscopy (EIS) test data or directly from measurements as voltage, current or temperature [32]. The EIS is a non-invasive method that characterizes the impedance through a wide frequency spectrum with the limitation that measurements are noisy, and requires expensive equipment usually found only in laboratories, restricting its application in practice [28], [33]. The second case of fuzzy logic methods represents a reasonable way for online SOC estimation and uncertainty characterization, but even so the SOC prediction is still unresolved and mainly treated as a curve regression problem which is insufficient for purposes of risk characterization. Neural Networks has also been used to estimate the SOC of a battery by nonlinear empirical models created as a relation between the measurements and the SOC. Train and validation data are required to generate and adjust the model, that can be used for estimation or prognostic purposes. However, these models can present overadjustment to the training and validation data, and the results may correspond to local optima [1], [26], [28].

In recent years there has been a growing interest in the use of stochastic filtering techniques as the extended Kalman filter (EKF) [34] to estimate the SOC and/or parameter degradation of a Li-Ion battery under a randomly varying loading conditions. The EKF is based on a non-linear battery model, like an equivalent circuit, and approximates the covariance error matrix associated to the state estimation using both the non-linear and linearization of the dynamic systems that represents the battery discharge process. During the estimation process the EKF adjust the parameters and model states as new measurement are available, but for prognostics for n-step ahead linearization errors are overly important to be neglected

[1], [26], [32], [33]. Although, SOC prognostics is still a research field with many unanswered questions.

Sequential Monte Carlo methods (SMC) (also known as particle filters (PF)) has shown a good performance in estimation and prediction processes with non-linear and non-necessary Gaussian noises [35]. In particular, SMC have been applied to the SOC estimation and prediction problem [28], [33], [36], [37]. These methods also provide a concrete characterization of uncertainty sources both in the filtering and the prediction stage, a piece of information that is required for the generation of a risk measure associated to SOC prognosis. Bayesian estimators require a state-space model for the dynamic system, and prognostic modules based on a state-space formulation for the dynamic system are very sensitive to the initial condition of the state vector. For this reason, the implementation of accurate online SOC estimators is absolutely relevant for the development of real-time predictors capable of quantifying the feasibility (as well as the cost) of a particular vehicle trajectory.

2.2.2 State-of-Health Estimation and Prognosis

As mentioned in Section 2.1.2, the SOH is usually characterized by the internal impedance, capacity fade, power fade and/or self discharge time, in either charge or discharge processes. When battery aging was discussed, it was exposed that aging is affected by various related factors that take place at similar timescales. This complexity and the fact that the SOH cannot be measured, implies that it has to be inferred from other observed and inferred values.

Most of the common solutions for the SOH estimation problem are limited to measure the battery terminal's voltage, or using methods as Coulomb counting and EIS measurements for each operation cycle. On the one hand, Coulomb counting requires an absolute knowledge about the future current provided by the ESD to predict the evolution of the SOH in an exact manner and to calibrate the measurement with respect to a reference point. On the other hand, changes in the internal impedance measurements can be used to estimate the degradation of the SOH, but the internal impedance has shown to be noisy and depends directly on the temperature, making it difficult to estimate reliably the SOH and generate long-term predictions about it. Besides, the EIS test is difficult to implement in practical applications (as seen on Section 2.2.1).

Research on SOH estimation has also focused on modeling the electro-chemical behavior of the accumulators [1], [38], building equivalent circuits, or studying the relationship between ESD degradation and a set of specific features (SOC, DOD, or the accumulator age). However, the analysis of the degradation processes also requires the incorporation of predictive models for the implementation of a scheme capable of performing simultaneously filtering (analysis of current state) and prognostic (analysis of future behavior) of the SOH. These predictive models need to incorporate the capability of parameter adaptation to minimize the effect of measurement inaccuracies on erroneous SOH estimates, as well as incorporating

changes in environmental and operating conditions within long-term predictions [39], [37], [40].

Fuzzy models and neural networks have also been used to estimate the SOH of Li-Ion batteries [41], although both approaches present inaccuracies originated from uncertainty sources that are present in nonlinear systems. Suboptimal Bayesian estimation techniques such as the extended Kalman filter (EKF) may be implemented for SOH prognosis when Coulomb counting methods are used to estimate the ESD SOH (providing adequate initial conditions for predictive models). The problem arises when trying to propagate this estimate in time in n-step ahead predictions: approximation errors are too significant to be neglected [35]. In [42], the concept of Bayesian estimation in combination with Monte Carlo methods is used to update the parameters of an empirical model, thus representing the prediction of the degradation process via PDF's.

Sequential Monte Carlo methods represent a concrete opportunity for algorithm improvement, since they have proved to be useful when trying to represent uncertainty in the prognosis of other nonlinear degradation processes [35], [37]. Some ESD (e.g., Li-ion batteries) however, suffer sudden a regeneration (or self-recharge) phenomena [37], [39], that directly affects the precision and accuracy of that type of algorithms. This is a fact that has only been briefly mentioned and studied in the current state-of-the-art. The statistical characterization of those phenomena has been incorporated within non-linear stochastic state-space models for SOH prognostic frameworks based on sequential Monte Carlo methods in [43], but neglecting the effect of an important variable, the operation temperature of the ESD.

Despite of the existence of Li-Ion battery degradation models that includes the operation temperature as an input [44], most of the described techniques consider an invariant temperature of approximately 23^oC. Fluctuations on the ambient or battery's temperature affects directly the capacity delivered by the ESD during a cycle, and can lead to erroneous estimations and predictions of the SOH. Lam *et al.* [45] uses the concept of usable Capacity to model the battery behavior, making a transformation of the battery's capacity at any temperature to a battery's capacity at a reference temperature. Hence, if the battery delivers much less energy due to an operation in low temperature environment, the model will not consider the battery degraded. In this sense, it is necessary to count with a scheme that allows the estimations and prognosis stages with the considerations previously explained, in addition to the incorporation of the effect of the temperature.

2.3 Bayesian Inference and Monte Carlo Methods

Errors associated to the SOC estimates are not so relevant for some devices as smartphones or laptops, because a SOC miscalculation may not lead to a harmful result. However, there are some critical applications where a poor SOC estimation can cause a catastrophic event.

Consider the example of an Unmanned Aerial Vehicle (UAV); an erroneous estimation of the SOC may cause the destruction of the device due to a crash landing, when forcing the UAV to flight when the battery may not provide the required power. This concept also applies for the SOH, and a good examples are the electrical and hybrid vehicles. The SOH gives information about the moment when the pack has to be replaced, or as an extra parameter during the purchase or sell of these cars.

The SOC and the SOH cannot be directly measured from the ESD, and do not present a direct relation with other variables that can be measured during the battery operation (at least for Li-Ion technology). As a consequence, it is necessary to make statistical inferences about them from other sensed signals or inferred values, as well as battery terminal voltages, current provided by the ESD, surface temperature for each cell, ambient temperature, depth of discharge, degradation of the ESD, time elapsed between cycles, among others. These reasons leads to the usage of Bayesian inference.

2.3.1 Bayesian Inference

The concept of Bayesian inference corresponds basically to the process of making statistical inferences of some variables using Bayes' Theorem. The conditional distribution of these variables given observations can be obtained from probability distributions for all relevant variables and the observations [46].

In the most common case, with the random variables A and B, the Bayes Rule is as follows:

$$P(A|B) = \frac{P(B|A)P(A)}{P(B)}. \tag{2.4}$$

The probability $P(A)$, or *prior distribution*, summarizes a set of beliefs or state of knowledge in hand before any observations are taken. The term $P(B|A)$, or *likelihood function*, characterizes the information carried by the observations [46]. In some applications, where $P(B)$ is fixed, then Bayes rule leads to a proportion between $P(A|B)$ and $P(B|A)P(A)$.

$$P(A|B) \propto P(B|A)P(A). \tag{2.5}$$

Many problems can be described in terms of a state space form, as shown in Equation (2.6), including electrical systems or time series analysis. The transition equation (2.6a) describes the *prior* distribution of a hidden Markov process and the observation (2.6b) describes the likelihood. Given a set of trajectories $x_{0:k} \triangleq \{x_0, x_1, ..., x_k\}\,; k \in \mathbb{N}$ and a set of observations $y_{0:k} \triangleq \{y_0, y_1, ..., y_k\}\,; k \in \mathbb{N}$, in a Bayesian framework the information about $x_{0:k}$ can be obtained from the posterior distribution $p(x_{0:k}|y_{0:k})$.

$$x_{k+1} = f(x_k, \omega_k) \tag{2.6a}$$

$$y_k = h(x_k, v_k). \tag{2.6b}$$

It can also be of interest to estimate recursively in time relations as the posterior marginal (called filtering distribution $p(x_k|y_{0:k})$), a prediction distribution $p(x_{k+j}|y_{0:k})$ for $j > k$, and expectations of the form of (2.7)

$$I(f_n) = \int f_n(x_{0:n}) p(x_{0:n}|y_{0:n}) \mathrm{d}x_{0:n}, \tag{2.7}$$

for any function $f_n : \mathbb{R}^{(n+1)\times n_x} \to \mathbb{R}$ integrable with respect to $p(x_{0:n}|y_{0:n})$. These integral allows to represent the moments of the process $x_{0:n}$ depending on the functions f_n.

The Bayesian relation given in (2.4) can be applied to the system previously described, resulting in the relation for the distributions

$$p(x_{0:k}|y_{0:k}) = \frac{p(y_{0:k}|x_{0:k})p(x_{0:k})}{p(y_{0:k})}. \tag{2.8}$$

Considering a system as (2.6), a recursive relation for $p(x_k|y_{0:k})$ can be derived from (2.8) [47].

$$p(x_k|y_{0:k}) = \frac{p(y_{0:k}|x_k)p(x_k)}{p(y_{0:k})} \tag{2.9}$$

$$p(x_k|y_{0:k}) = \frac{p(y_k, y_{0:k-1}|x_k)p(x_k)}{p(y_k, y_{0:k-1})} \tag{2.10}$$

$$p(x_k|y_{0:k}) = \frac{p(y_k|y_{0:k-1}, x_k)p(y_{0:k-1}|x_k)p(x_k)}{p(y_k|y_{0:k-1})p(y_{0:k-1})} \tag{2.11}$$

$$p(x_k|y_{0:k}) = \frac{p(y_k|y_{0:k-1}, x_k)p(x_k|y_{0:k-1})p(y_{0:k-1})p(x_k)}{p(y_k|y_{0:k-1})p(y_{0:k-1})p(x_k)} \tag{2.12}$$

$$p(x_k|y_{0:k}) = \frac{p(y_k|x_k)p(x_k|y_{0:k-1})}{p(y_k|y_{0:k-1})}. \tag{2.13}$$

Then, the recursive relation is given by (2.14):

$$\overbrace{p(x_k|y_{0:k})}^{posterior} = \frac{\overbrace{p(y_k|x_k)}^{likelihood} \cdot \overbrace{p(x_k|y_{0:k-1})}^{prior}}{\underbrace{p(y_k|y_{0:k-1})}_{Evidence}}. \tag{2.14}$$

Using the Chapman-Kolmogorov equation, the denominator $p(y_k|y_{0:k-1})$ can be expressed as

$$p(y_k|y_{0:k-1}) = \int p(y_k|x_k)p(x_k|y_{1:k-1})\mathrm{d}x_k, \tag{2.15}$$

and a theoretical solution exists for the Bayesian estimation, but it cannot be assured that the integrals have analytical solution.

If the relations that defines the dynamic model given by the state equations of the form (2.6b) and (2.6a) are linear and affected by Gaussian noises, then its possible to obtain an optimum analytical expression for the evolution of the *a posteriori* distribution (in the sense of the mean squared error). This expressions correspond to the Kalman filter [48]. However, when the processes are non-linear with non-necessarily Gaussian noises, and with a high dimensionality, the sequence of *a posteriori* density are multidimensional integrals with non-linear arguments that do not present explicit solution for the general case. In this case, it is possible to implement approximated methods as the extended Kalman filter, unscented Kalman filter, or numeric methods as the sequential Monte Carlo (Particle filter) [34], [35].

2.3.2 Sequential Monte Carlo Methods: Particle Filters

Monte Carlo methods solves the problem of Bayesian estimation replacing complex analytic or unknown probability distributions with sample-based representations [49]. Given a generic probability density $\pi_k(x_{0:k})$, and N independent random variables sampled from $x_{0:k}^{(\mathrm{i})} \sim \pi_k(x_{0:k})$ for $\mathrm{i} = 1, ..., N$, the Monte Carlo method approximates $\pi_k(x_{0:k})$ by the empirical measure in the equation (2.16), where $\delta(\cdot)$ is the Dirac delta function [50].

$$\hat{\pi}_k(x_{0:k}) = \frac{1}{N} \sum_{\mathrm{i}=1}^{N} \delta(x_{0:k} - x_{0:k}^{(\mathrm{i})}) \tag{2.16}$$

Sequential Monte Carlo methods or Particle Filter (PF) is a technique to implement Bayesian estimations by Monte Carlo simulations, using the Importance Sampling method. Given a state-state representation with the states $x_{0:k}$ and the observations $y_{0:k}$, the principal idea of the PF is to represent the posterior distribution $p(x_{0:k}|y_{0:k})$ by a set of N_p weighted particles $\left\{w_k^{(\mathrm{i})}, x_{0:k}^{(\mathrm{i})}\right\}$ or point masses, where the particles are random samples of the unknown states, and the weights are probability masses estimated using the Bayes recursion [49]. The equation (2.17) shows the empirical distribution that approximates the analytical posterior distribution.

$$p(x_{0:k}|y_{0:k}) \approx \sum_{\mathrm{i}=1}^{N_p} w_k^{(\mathrm{i})} \delta(x_{0:k} - x_{0:k}^{(\mathrm{i})}) \tag{2.17}$$

This approximations can be used to estimate the expectations of any function of interest $f_n(x)$ integrable with respect to $p(x_{0:k}|y_{0:k})$, as the presented in Equation (2.7).

Importance Sampling (IS)

This section and the following considers the particular case of state-space models used for Bayesian estimation purposes.

A problem that Monte Carlo methods present is that if the target distribution $\pi_k(x_{0:k})$ is a complex high-dimensional probability distribution, or is unknown, then samples can not be obtained from it. The Importance Sampling method allows computations of expectations with respect to one target distribution using random samples drawn from another distribution, $q_k(x_{0:k})$ [49], [50]. The distribution $q_k(x_{0:k})$ is referred as *importance sampling distribution* as it samples $\pi_k(x_{0:k})$ non uniformly giving different "importance" to some values of $\pi_k(x_{0:k})$ than others. A necessary condition for importance sampling is that

$$\pi_k(x_{0:k}) > 0 \Rightarrow q_k(x_{0:k}) > 0. \tag{2.18}$$

Consider the case of estimate the expectation of a function $\phi(x)$ for $x \sim \pi(x)$. This integral can be treated as

$$\begin{aligned} E\{\phi(x)\} &= \int_X \phi(x)\pi(x)\mathrm{d}x & (2.19)\\ &= \int_X \phi(x)\left(\frac{\pi(x)}{q(x)}\right)q(x)\mathrm{d}x \quad \text{for } \int q(x)\mathrm{d}x = 1. & (2.20) \end{aligned}$$

An importance sample estimator is obtained sampling $x^{(\mathrm{i})}, \mathrm{i} = 1, ..., N$ from the importance distribution $q(x)$ and computing the sample mean. Approximating $q(x)$ as $\hat{q}(x) \approx \sum_{\mathrm{i}=1}^{N} \delta(x - x^{(\mathrm{i})})$, then the expectation of the equation (2.20) can be expressed as

$$E\{\phi(x)\} \approx \frac{1}{N}\sum_{\mathrm{i}=1}^{N} \phi(x^{(\mathrm{i})})\left(\frac{\pi(x^{(\mathrm{i})})}{q(x^{(\mathrm{i})})}\right). \tag{2.21}$$

The idea is to choose the importance distribution as similar as possible to the target distribution $\pi(x)$. This concept of importance sampling can be used to the Bayesian estimation problem in cases when it is not possible to obtain samples directly from the posterior distribution. Choosing an importance sampling $q(x_{0:k}|y_{0:k})$, expectations of functions ϕ of $x_{0:k}$ can be expressed as

$$\begin{aligned} E\{\phi(x)\} &= \int_X \phi(x_{0:k})p(x_{0:k}|y_{0:k})\mathrm{d}x & (2.22)\\ &= \int_X \phi(x_{0:k})\left(\frac{p(x_{0:k}|y_{0:k})}{q(x_{0:k}|y_{0:k})}\right)q(x_{0:k}|y_{0:k})\mathrm{d}x_{0:k}. & (2.23) \end{aligned}$$

Defining weights as the reason $\bar{w}_{0:k} \equiv p(\cdot)/q(\cdot)$, and applying Bayes' rule, then

$$\bar{w}_{0:k} = \frac{p(x_{0:k}|y_{0:k})}{q(x_{0:k}|y_{0:k})} = \frac{p(y_{0:k}|x_{0:k})p(x_{0:k})}{p(y_{0:k})q(x_{0:k}|y_{0:k})}. \tag{2.24}$$

When $p(y_{0:k}) = \int p(y_{0:k}|x_{0:k})p(x_{0:k})\mathrm{d}x_{0:k}$ is not available, a new weight can be defined

$$w_{0:k} = \frac{p(y_{0:k}|x_{0:k})p(x_{0:k})}{q(x_{0:k}|y_{0:k})} \propto \bar{w}_{0:k}. \tag{2.25}$$

Replacing the weights' equation (2.25) into equation (2.23), the expectation is $E\{w_{0:k}\phi(x_{0:k})\}$ scaled by a normalizing constant

$$E_q\{\phi(x)\} = \frac{1}{p(y_{0:k})}\int_X \phi(x_{0:k})\left(\frac{p(y_{0:k}|x_{0:k})p(x_{0:k})}{q(x_{0:k}|y_{0:k})}\right)q(x_{0:k}|y_{0:k})\mathrm{d}x_{0:k} \quad (2.26)$$

$$= \frac{1}{p(y_{0:k})}\int_X \phi(x_{0:k})w_{0:k}q(x_{0:k}|y_{0:k})\mathrm{d}x_{0:k} \quad (2.27)$$

$$= \frac{E\{w_{0:k}\phi(x_{0:k})\}}{p(y_{0:k})}. \quad (2.28)$$

From the equation (2.25) a relation for the observation probability can be obtained multiplying the weights by the importance distribution and integrating with respect to $x_{0:k}$

$$\int w_{0:k}q(x_{0:k}|y_{0:k})\mathrm{d}x_{0:k} = \int p(y_{0:k}|x_{0:k})p(x_{0:k})\mathrm{d}x_{0:k} \quad (2.29)$$

$$= p(y_{0:k}), \quad (2.30)$$

and the expectation of $\phi(x_{0:k})$ is

$$E\{\phi(x)\} = \frac{E_q\{w_{0:k}\phi(x_{0:k})\}}{\int w_{0:k}q(x_{0:k}|y_{0:k})\mathrm{d}x_{0:k}} \quad (2.31)$$

$$= \frac{E_q\{w_{0:k}\phi(x_{0:k})\}}{E_q\{w_{0:k}\}}. \quad (2.32)$$

Sampling from $x_{0:k} \sim q(x_{0:k}|y_{0:k})$ and using the sampling distribution, $\hat{q}(x_{0:k}|y_{0:k}) \approx \frac{1}{N}\sum_{\mathrm{i}=1}^{N}\delta(x_{0:k} - x_{0:k}^{(\mathrm{i})})$, and defining the normalized weights $\tilde{\omega}_{0:k}^{(\mathrm{i})} = \frac{w_{0:k}^{(\mathrm{i})}}{\sum_{\mathrm{i}=1}^{N} w_{0:k}^{(\mathrm{i})}}$, then the final estimate of the expectation is

$$E\{\phi(x)\} \approx \sum_{\mathrm{i}=1}^{N} \tilde{\omega}_{0:k}^{(\mathrm{i})}\phi(x_{0:k}^{(\mathrm{i})}). \quad (2.33)$$

This estimator is biased because is the result of the division of two estimators, but under weak assumptions, the strong law of the large number applies, converging asymptotically to the true statistic [51]. As the number N of samples increase, an asymptotically optimal estimate of the posterior is

$$\hat{p}(x_{0:k}|y_{0:k}) \approx \sum_{\mathrm{i}=1}^{N} \tilde{\omega}_{0:k}^{(\mathrm{i})}\delta(x_{0:k} - x_{0:k}^{(\mathrm{i})}). \quad (2.34)$$

Sequential Importance Sampling and Resampling

The Importance Sampling algorithm solves the problem when it is not possible to sample from a high-dimensional probability distribution. However, even if it is possible to sample exactly

from $p_k(x_{0:k}|y_{0:k})$, the computational complexity of such a sampling scheme is tipically at least linear in the number of variables k. With a sampling algorithm that samples sequentially for each k, then the computational complexity increase at least linearly with k [50].

A recursive algorithm can be derived to avoid the necessity of high computational resources in the estimation of the posterior density $p(x_{0:k}|y_{0:k})$, where at each instant k the previous state samples $x^{(\mathrm{i})}_{0:k-1}$, and the samples of the state $x^{(\mathrm{i})}_k$ are obtained only from the observation y_k and the previous estimation of the filter density $p(x_{0:k-1}|y_{0:k-1})$.

This solution involves selecting an importance distribution $q(x_{0:k}|y_{0:k})$ that admits the importance distribution of the previous instant $q(x_{0:k-1}|y_{0:k-1})$ as the marginal distribution, as presented in equation (2.36).

$$q(x_{0:k}|y_{0:k}) = q(x_{0:k-1}|y_{0:k-1})q(x_k|x_{0:k-1}, y_{0:k}) \tag{2.35}$$

$$q(x_{0:k}|y_{0:k}) = q(x_0|y_0)\prod_{j=1}^{n} q(x_j|x_{0:j-1}, y_{0:j}). \tag{2.36}$$

With the selected importance sampling distribution, it is possible to obtain a sample $x^{(\mathrm{i})}_{0:k}$ without modifying the previous sample $x^{(\mathrm{i})}_{0:k-1}$, it means:

$$x^{(\mathrm{i})}_k \sim q(x_k|x^{(\mathrm{i})}_{0:k-1}). \tag{2.37}$$

The equations (2.25) and (2.36) leads to a recursive expression for the importance weight (2.38).

$$\tilde{\omega}^{(\mathrm{i})}_k \propto \tilde{\omega}^{(\mathrm{i})}_{k-1}\frac{p(y_k|x^{(\mathrm{i})}_k)p(x_k|x_{k-1})}{q(x_k|x_{0:k-1}, y_{0:k})} \tag{2.38}$$

The approach of the SIS algorithm solves the IS problem recursively in a more efficient form. However, the variance of the importance weights can only increase for importance sampling distributions that satisfies (2.36) [52]. This leads in a few iterations to a scenario where only a singular particle presents a non-zero weight value. This problem is called degeneracy. A strategy to limit the algorithm degeneracy is to consider the importance distribution that minimizes the variance of the importance weights conditional upon the simulated trajectory $x^{(\mathrm{i})}_{0:k-1}$ and the observations $y_{0:k}$ [52].

Two propositions are presented in [52] that are related to the degeneracy of the algorithm:

- **Proposition 1:** *"The unconditional variance of the importance weights, i.e. with the observations $y_{0:k}$ being interpreted as random variables, increases over time."*

- **Proposition 2:** *"$q(x_k|x^{(\mathrm{i})}_{0:k-1}, y_{0:k}) = p(x_k|x^{(\mathrm{i})}_{k-1}, y_k)$ is the importance function which minimizes the variance of the importance weight $\omega^{*(\mathrm{i})}_k$ conditional upon $x^{(\mathrm{i})}_{0:k-1}$ and $y_{0:k}$."*

The choice of the importance distribution is critical for the performance of the particle filter scheme, and has to be considered as a design parameter of the filter. A simple choice uses the prior distribution of the hidden Markov model as importance function, it means select $q(x_{0:k}|y_{0:k}) = p(x_k|x_{k-1})$, and a recursion for the weights of the form $\tilde{\omega}^{*(\mathrm{i})}_{0:k} \propto \tilde{\omega}^{*(\mathrm{i})}_{0:k-1} p(y_k|x^{(\mathrm{i})}_{0:k})$.

Resampling

Both IS and SIS algorithms provide estimates with increasing variance over time. Resampling techniques solve this problem partially, eliminating the trajectories with small normalized weights (low likelihood) and concentrating upon those with large weights. A measure of the degeneracy of the algorithm is the effective sample size N_{eff} (2.39), and because it cannot be evaluated directly, an estimate is used $\hat{N}_{eff}$ (2.41) [52].

$$N_{\mathrm{e}ff} = \frac{N}{1 + var_{q(\cdot|y_{0:k})}(\tilde{\omega}^(x_{0:k}))} \tag{2.39}$$

$$= \frac{N}{\mathbb{E}_{q(\cdot|y_{0:k})}\left[((\tilde{\omega}^(x_{0:k})))^2\right]} \leq N \tag{2.40}$$

$$\hat{N}_{\mathrm{e}ff} = \frac{1}{\sum_{\mathrm{i}=1}^{N} (\tilde{\omega}^{(\mathrm{i})}_k)^2} \tag{2.41}$$

The resampling procedure is used when the estimate of the effective numbre of particles $\hat{N}_{eff}$ is lower than a fixed threshold. The three most popular resampling algorithms are the "systematic resampling", "residual resampling", and "multinomial resampling". It is important to mention that in this resampling scheme, the new weights have all the same value $1/N$, where N is the number of particles.

Despite of the resampling procedure decrease algorithmically the degeneracy of the particles, it also introduces some theoretical and practical problems. Theoretically, this resampling routine removes the statistical independence of the samples, and the simple convergence of the MC scheme is lost. From a practical point of view, the resampling method combines all the particles limiting the chance to parallelize [52]. An importance advantage of resampling is that it allows to remove the particles with low weight with high probability, allowing to focus the computational efforts on the regions with high probability mass in a sequential scheme [50].

2.3.3 A Particle-filtering-based Prognosis Scheme for non-linear Dynamic Systems

Prognosis schemes can be understood basically as the result of long-term predictions describing the evolution of a fault indicator, with the purpose of estimate the Remaining Useful Life (RUL) of a component or system, from the initial conditions given by the estimation step.

The prediction of critical events require the existence of at least one critical component that provides the severity of the studied condition. It is always possible to combine different characteristics to obtain one unique signal. Then, it is possible to describe the evolution in time of the dimension of the fault, which is associated to the observed degradation variable of the component, through non-linear state equations.

For the generation of long-term predictions, consider the m-step prediction for the conditional state PDF $\hat{p}(x^{(\mathrm{i})}_{k+\tau}|\hat{x}^{(\mathrm{i})}_{k+\tau-1})$ which describes the state distribution at the future instant $k+\tau, (\tau = 1, ..., m)$ when the particle $\hat{x}^{(\mathrm{i})}_{k+\tau-1}$ is used as initial condition. With the assumption that the current weights $\left\{\tilde{\omega}^{(\mathrm{i})}_{k}\right\}_{\mathrm{i}=1,...,N}$ are a good representation of the state PDF at time k, then it is possible to approximate the predicted state PDF at time $k+\tau$, by using the law of total probabilities and the particle weights at time $t+\tau-1$, as shown in (2.42).

$$\hat{p}(x_{k+\tau}|\hat{x}_{1:k+\tau-1}) \approx \sum_{\mathrm{i}=1}^{N} \tilde{\omega}^{(\mathrm{i})}_{k+\tau-1} \cdot \hat{p}(x^{(\mathrm{i})}_{k+\tau}|\hat{x}^{(\mathrm{i})}_{k+\tau-1}); \quad \tau = 1, ..., m. \tag{2.42}$$

Considering the prediction problem, the weight update cannot depend on the acquisitions of new measurements. This consideration has to be taken account to evaluate (2.42), where the weight of every particle should be modified at each prediction step to include the fact that noise and process non-linearities could change the shape of the PDF at time pases. Part of the prediction problem is to search reliable approximations where the prediction scheme does not depend on new data.

To overcome most of these difficulties, this subsection presents two approaches that has been developed and evaluated in [35]. The first approach uses the value of the particles obtained from the filtering step as the initial condition to generate m-step predictions of the expected value of the states PDF. The second approach considers a resampling of the predicted state PDF (2.42).

First Approach for m-step ahead long-term predictions

For this approach, the prediction of the evolution in time of each particle is made by successively taking the expectation of the model update equation (2.6a) for each future time

instant, considering the state value associated to that particle as initial condition, as shown in

$$\hat{x}_{k+\tau}^{(\mathrm{i})} = E\left[f_{k+\tau}(\hat{x}_{k+\tau-1}^{(\mathrm{i})}, \tilde{\omega}_{k+\tau})\right] \tag{2.43}$$

Although the advantage of being the simplest implementation in terms of computational efforts, this method present problems related to the assumption that (2.43) is sufficient to extend the trajectories $\hat{x}_{0:k+\tau}^{(\mathrm{i})}$ while the current particle weights are propagated in time without changes. Moreover, it does not take into account the existence of other uncertainty sources involved in practical applications, as model inaccuracies or even wrong hypothesis.

Second Approach for m-step ahead long-term predictions

The second approach presented is a prognosis scheme based on the regularized particle filter [51], in which instead of recalculating the weights of the particles, it proposes a representation of the future uncertainty by resampling the predicted state PDF. This approach is especially useful if the prediction horizon is large.

Consider the discrete approximation (2.44) for the predicted state PDF (2.42) where $K(\cdot)$ is a kernel density function, which may correspond to the process noise PDF, a Gaussian kernel or a rescaled version of the Epanechnikov kernel (2.45), with the bandwidth h_{opt} (2.46), and the rescaled regularisation kernel (2.47). c_{n_x} corresponds to the volume of the unit sphere in $\mathbb{R}^{n_x}$ [35].

$$\hat{p}(x_{k+\tau}|\hat{x}_{1:k+\tau-1}) \approx \sum_{\mathrm{i}=1}^{N} \omega_{k+\tau-1}^{(\mathrm{i})} K_h\left(\hat{x}_{k+\tau} - E\left[\hat{x}_{k+\tau}^{(\mathrm{i})} - \hat{x}_{k+\tau-1}^{(\mathrm{i})}\right]\right), \tag{2.44}$$

$$K(x) = \begin{cases} \frac{n_x+2}{2c_{n_x}}(1-||x||^2) & \mathrm{i}f||x|| < 1 \\ 0 & otherwise \end{cases} \tag{2.45}$$

$$h_{opt} = A \cdot N^{-\frac{1}{n_x+4}}; \quad A = \left(8c_{n_x}^{-1} \cdot (n_x+4) \cdot (2\sqrt{\pi})^{n_x}\right)^{\frac{1}{n_x+4}} \tag{2.46}$$

$$K_h = \frac{1}{h^{n_x}} K\left(\frac{x}{h}\right), \tag{2.47}$$

This method proposes a computationally affordable solution based on the assumption of uncorrelated process noise and the use of kernel transitions to describe the state PDF before the resampling step. To complete this task, a new population of equally weighted particles is generated for the instant $k = 1, ..., m$, performing an inverse transform resampling procedure for the particle population. Hence, the information about the distribution of the state is given by the position of the particles instead of their weight value. It is important to mention that the assumption of uncorrelated process noise is included for the sake of

reducing the computational effort of the resampling procedure, and there are no theoretical restrictions for the application of this methodology in the presence of correlated process noise.

An additional step is considered to avoid loss of diversity among particles. It is assumed that the state covariance matrix $\hat{S}_{k+\tau}$ is equal to the empirical covariance matrix of $\hat{x}_{k+\tau}$ and that a set of equally weighted samples for $\hat{x}_{k+\tau-1}$ is available.

With all the aforementioned considerations, the regularization algorithm is as follows [35]:

Long-term predictions: second approach

- Apply modified inverse transform resampling procedure. For $\mathrm{i} = 1, ..., N$, $\tilde{\omega}^{(\mathrm{i})}_{k+\tau} = N^{-1}$.
- Calculate $\hat{S}_{k+\tau}$, the empirical covariance matrix of $\left\{E\left[\hat{x}^{(\mathrm{i})}_{k+\tau} \mid \hat{x}^{(\mathrm{i})}_{k+\tau-1}, \tilde{\omega}^{(\mathrm{i})}_{k+\tau}\right]\right\}_{\mathrm{i}=1,...,N}$
- Compute $\hat{D}_{k+\tau}$ such that $\hat{D}_{k+\tau}\hat{D}^{T}_{k+\tau} = \hat{S}_{k+\tau}$
- For $\mathrm{i} = 1, ..., N$, draw $\varepsilon^{\mathrm{i}} \sim K$, the Epanechnikov kernel and assign $\hat{x}^{(\mathrm{i})*}_{k+\tau} = \hat{x}^{(\mathrm{i})}_{k+\tau} + h^{opt}_{k+\tau}\hat{D}_{k+\tau}\varepsilon^{\mathrm{i}}$, where $h^{opt}_{h+\tau}$ is computed as in (2.45).

Estimation and Statistical Characterization of the Remaining Useful Life

The resulting predicted state PDF contains critical information about the evolution of the fault dimension over time. One way to represent that information is through the computation of statistics as expectations or 95% confidence intervals, for either the End-of-Life (EOL) or the Remaining Useful Life (RUL) of the faulty system. The EOL PDF depends on both long-term predictions and empirical knowledge about critical conditions for the system. This empirical knowledge is usually incorporated in the form of thresholds for main fault indicators. Therefore, the probability of failure at any future time instant $k = eol$ (namely the EOL PDF) is given by:

$$P\left(EOL = eol\right) = \sum_{\mathrm{i}=1}^{N} P\left(Failure | X = x^{(\mathrm{i})*}_{eol}\right) \cdot w^{(\mathrm{i})}_{eol} \tag{2.48}$$

The conditional probability of failure in (2.48) may be defined via the determination of hazard zones [35], either using historical data or knowledge from process operators. The simplest case is where the concept of *failure* implies the moment when the fault feature crosses a given threshold f_{th}. In that case the probability of failure, conditional to the state, is equal to one if the state is exactly on the manifold that defines the threshold value.

Two measures of the performance of prognostics algorithms are the expected EOL (2.49), which corresponds to the instant k when the expectation of the corresponding state reaches a failure condition, and the Just-in-Time Point $JITP_{\gamma\%}$ (2.50) value [53]. The latter measure

incorporates the concept of "risk", specifying the time instant where the probability of failure reaches a specified threshold γ. Figure 2.13 illustrate the concept of Just-in-Time point, showing the $JITP_{5\%}$ and $JITP_{15\%}$ for a PDF.

$$\hat{EOL} \triangleq E\{k|E\{x(k)\} = f_{th}\} \tag{2.49}$$

$$JITP_{\gamma\%} = \underset{eol}{argmin}\left(P\{EOL \leq eol\} > \gamma\%\right) \tag{2.50}$$

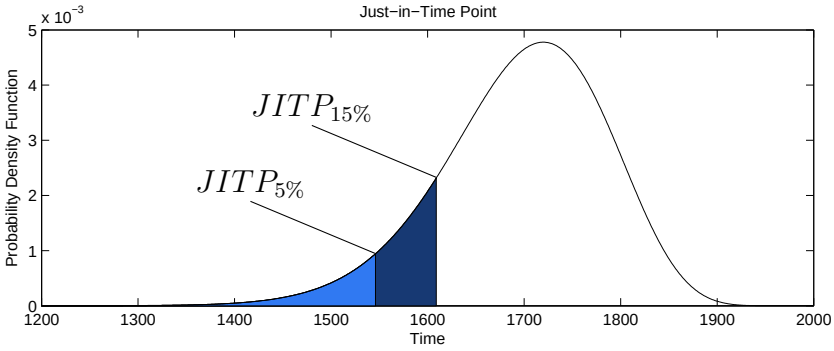

Figure 2.13: Just-in-Time Point (JITP) of 5% and 15% for a failure probability.

The definition of the EOL or the RUL depends on the specific case under supervision. When considering predictions about the SOC of an ESD, the EOL is associated to the end-of-discharge (EOD) value, usually characterized by the time instant when the battery voltage reach a specified threshold voltage. For the SOH prediction problem, it is considered by the cycle number when the battery capacity drops to a percentage of its nominal capacity (generally 80% or 85% of its nominal value).

Chapter 3

Laboratory Implementation and Data Acquisition

It is crucial to count with diverse ESD discharge and degradation data in order to generate estimates and long-term predictions for the evolution in time of the battery SOC and SOH, specially if the effect of the temperature is included. This reason motivates the generation of a data set of battery degradation under different temperatures of operation. In addition, other tests are necessary to characterize the behavior of the batteries in function of the ambient temperature.

In this work all the conducted tests were performed with individual Li-Ion cells. The laboratory equipment used to operate the batteries consists of two battery chargers iCharger 208B, and a programmable electronic load BK8500. To charge and discharge the cells at different temperatures, an adapted commercial thermoelectric cooler (TEC) based on the Peltier effect is used. The principal idea of this cooler is depicted in Figure 3.1. The temperature difference $\Delta T(\mathrm{i}(t))$ between the two sides of the Peltier module depends on the magnitude and sign of the current $\mathrm{i}(t)$ flowing through it. Then, if one side of the module is kept at room temperature (with a heat sink with a cooling fan), the other side can be over or below that temperature depending on the sign of the current. To operate the cells at room temperature, they are placed inside a PMMA box with temperature sensors.

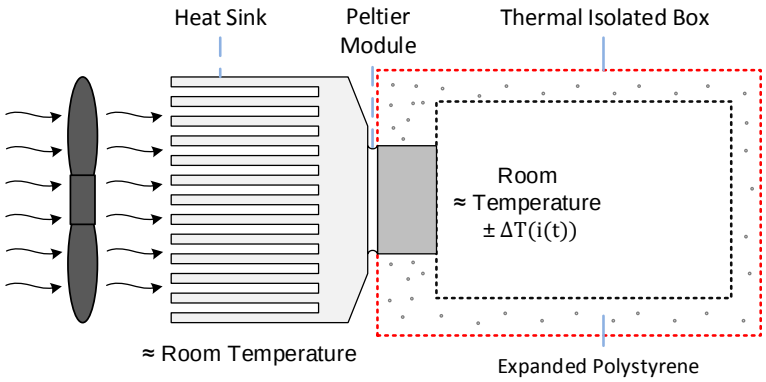

Figure 3.1: Illustration of the thermoelectric cooling system operation.

The temperature is sensed with NTC thermistors connected to a ©inex board providing a linear relation between the voltage measurements and the actual temperature in the range of -20^oC to 85^oC. The sensor placed at the battery is located near the negative pole of the cell where the maximum cell surface temperature is found [2]. The room temperature sensor is located at approximately $14[cm]$ over the battery.

Figure 3.2 shows the previously mentioned equipment, corresponding to the iCharger (A), Electronic Load (B), thermoelectric cooler (C), and PMMA box (B). The location of the thermistor on the battery case is shown in Figure 3.3. Figure 3.4 presents the interior of TEC, with the location of the battery case and the thermistor used to sense the ambient temperature.

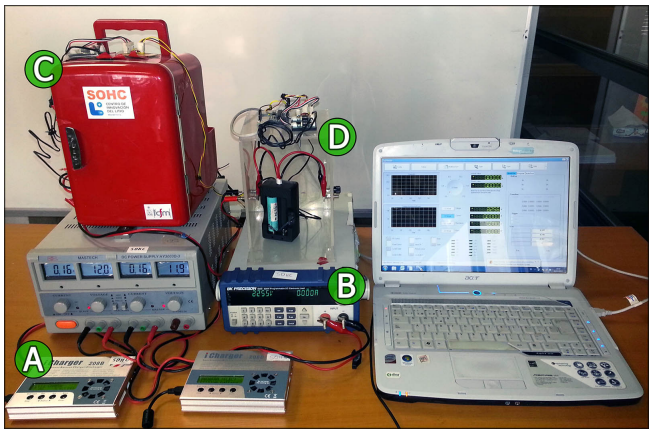

Figure 3.2: Photography of the equipment used to operate the Li-Ion cells.

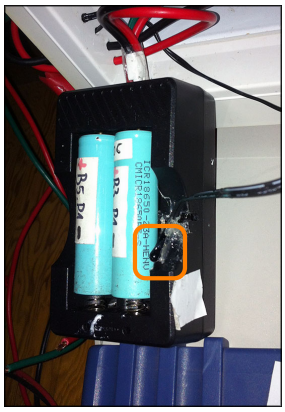

Figure 3.3: Photography of the battery case, showing with an orange circle the location of the sensor near to the negative pole.

Figure 3.4: Photography of the inside of the TEC, with the battery case and the temperature sensors.

3.1 Accelerated Degradation Data

Due to the limitation of time and the lack of an autonomous battery cycling equipment, in addition to fact that there is only one electronic load, only a limited amount of tests can be actually implemented during the time span associated with this work. In this way, it was defined that three different cells were going to be degraded under different temperatures of operation but similar conditions of accelerated degradation data set, so a high mean current and high DOD were considered.

The cells were obtained from an alternative laptop battery pack that consisted of six Li-Ion 18650 rechargeable cells of $3.7[V]$ and $2400[mAh]$. The temperatures of operation are: room, low ($\approx 3[^oC]$) and high ($\approx 40[^oC]$) temperature. The load cycle is adapted from an electric vehicle test and is explained in the following section.
The charging protocol is the typical CC-CV (See Section 2.1.2). In this case, batteries are charged with a CC of $2[A]$ and CV of $4.1[V]$, with a lower limit of $0.2[A]$ for the current in the CV stage. Moreover, the battery chargers are set with a cut-off time limit of 2 hours for security reasons.

3.1.1 Load Cycle Selection

Different load profiles may be carried out to study batteries, as there are many factors implied in the degradation mechanisms. Some of the most important effects on battery aging are the current levels, variations of the current over time, depth of discharge and temperature of operation.

In order to establish a load cycle test to study batteries degradation, an adaptation of the FUDS[†]-based battery power-time profile [54] specified by the United States Advanced Battery Consortium (USABC) was implemented. The purpose of the FUDS-based battery power profile is to test the battery under a variable power discharge regime that represents an actual power requirement from an electric vehicle. It considers discharge and charge processes with high power peaks. Figure 3.5 shows the FUDS-based test, where negative values corresponds to discharge and positive values to charge process.

As the goal is to generate and study accelerated degradation data with high currents and high DOD, then the FUDS has to be modified, with the changes listed as follows.

1. Charge power is replaced with a 0% value and discharge power multiplied by -1.

2. Power of 0% is considered as low current level and 100% as high current level.

3. Discharge power is quantized into eleven equally spaced levels, assigning the power

[†] Federal Urban Driving Schedule

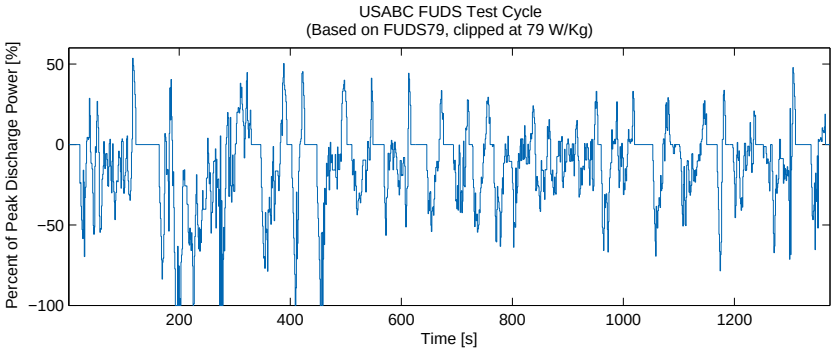

Figure 3.5: FUDS-based battery power-time test cycle.

value to the nearest level.

4. As an accelerated degradation is desired, low current is selected to be 2.6[A] and high current 3[A], because these values offer a range where the cells are operated over nominal values but under safe conditions. Then, current levels differ by 0.04[A]. The average current under these conditions is 2.66[A]. These changes can be seen in Figure 3.6. In addition, the cut-off voltage for discharge is considered to be 0.5[V] to achieve a deep discharge.

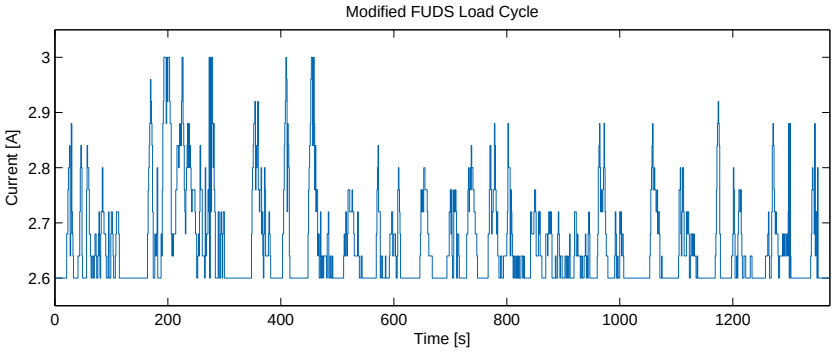

Figure 3.6: Scaled version of the FUDS-based battery power test cycle.

5. The FUDS is specified for 1372 seconds and the cell discharges are expected to last longer than that value. Hence, the load cycle is repeated until the battery is discharged.

6. Finally, a squared wave with period of 20 seconds is placed at the beginning of the load cycle. It is scaled to have a minimum value of 0.3[A] and maximum value of 1.5[A]. In addition, this signal lasts for 60 seconds as Figure 3.7 illustrates. These pulses are intended to study the evolution of the voltage drop due to internal impedance over battery cycling, without the necessity of extra equipment.

7. The described load cycle is used with low and high operation temperatures as shown in Figure 3.8.

8. For room temperature, some rest period were added, where the electronic load does not take energy from the battery. These disconnection periods last for 10 seconds and are separated by 500 seconds. Figure 3.9 exhibits the load cycle with these modifications.

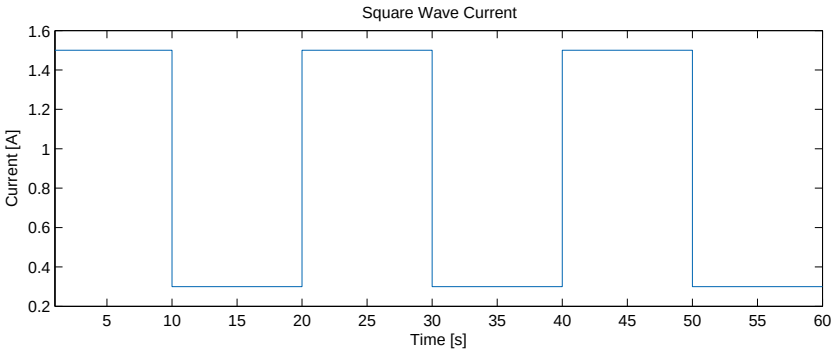

Figure 3.7: Square waves considered to estimate the internal impedance.

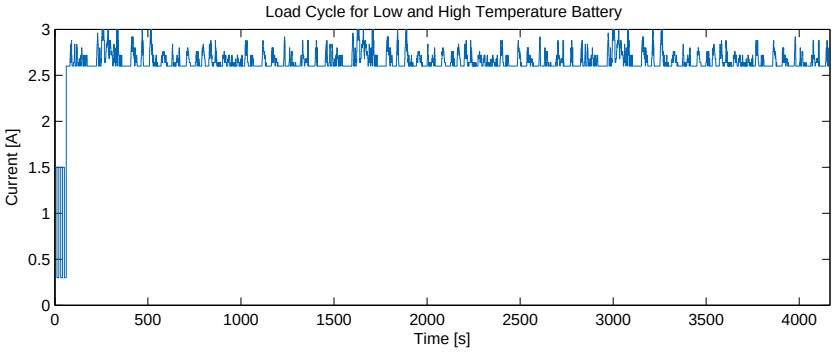

Figure 3.8: Load cycle for low and high temperature batteries.

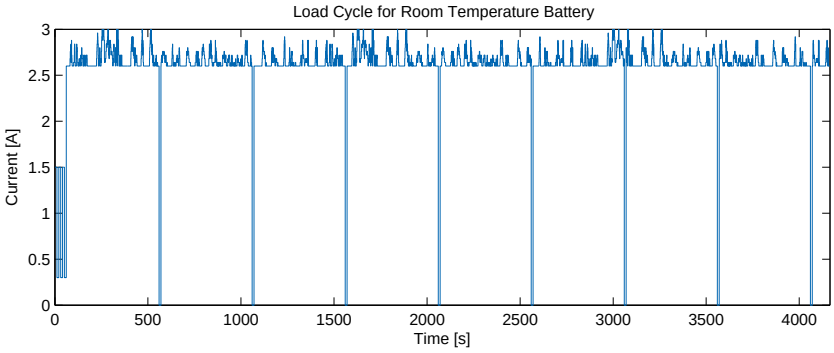

Figure 3.9: Load cycle for room temperature battery.

The principal idea of these load profiles is to operate the cells at a variable discharge current, attempting to assimilate the usage of the battery on a real application. Furthermore, some modifications were made in order to add useful information for the study of the behavior of the cell. For future degradation tests, it is proposed to generate data with temperatures outside the optimal range (see Figure 2.5), and degrade cells combining different temperatures of operation for each cycle. Also, combining these test proposal with variations on the DOD and current rates would be recommendable.

3.1.2 Generated Accelerated Degradation Data

The conditions of operation for the three cycled batteries is listed as follows:

- **Battery #4:**
  - Charged at $\approx 3^oC$.
  - Discharged at $\approx 3^oC$ with the load cycle shown in Figure 3.8.
- **Battery #5:**
  - Charged at $\approx 23^oC$.
  - Discharged $\approx 23^oC$ with the load cycle shown in Figure 3.9.
- **Battery #6:**
  - Charged at $\approx 23^oC$.
  - Discharged at $\approx 40^oC$ with the load cycle shown in Figure 3.8.

The results for the generation of accelerated degradation data are shown in Figures 3.10, 3.11 and 3.12 for Batteries #4, #5 and #6, respectively. Each figure presents the capacity of both charge and discharge process. For every twenty cycles of operation, there is a comparative cycle where the batteries are charged and discharged at room temperature, in order to establish a comparison point between them in terms of their degradation. They correspond to the 21^{st}, 41^{st}, 61^{st}, 81^{st} and 101^{st} cycles.

It is worth to mention that the average temperature of operation is not the same for each cycle, and is affected in a great form by the season and ambient temperature of each day. Figure 3.13 shows the charge mean temperature for each battery as a function of the cycle number.

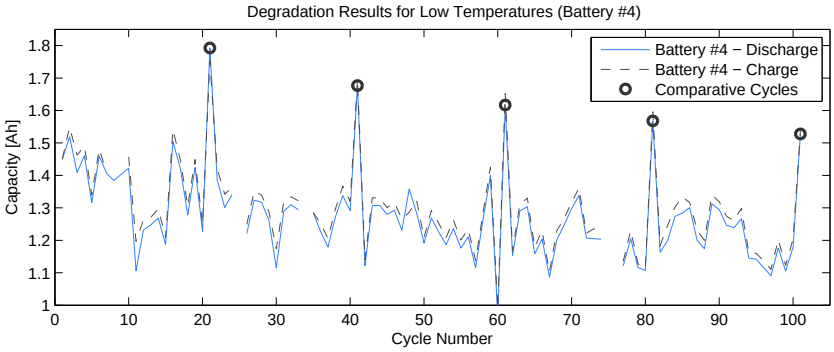

Figure 3.10: Degradation data obtained cycling Battery #4 at low temperature.

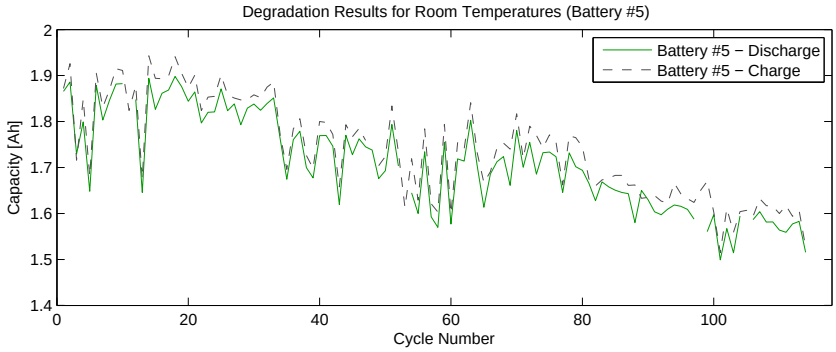

Figure 3.11: Degradation data obtained cycling Battery #5 at room temperature.

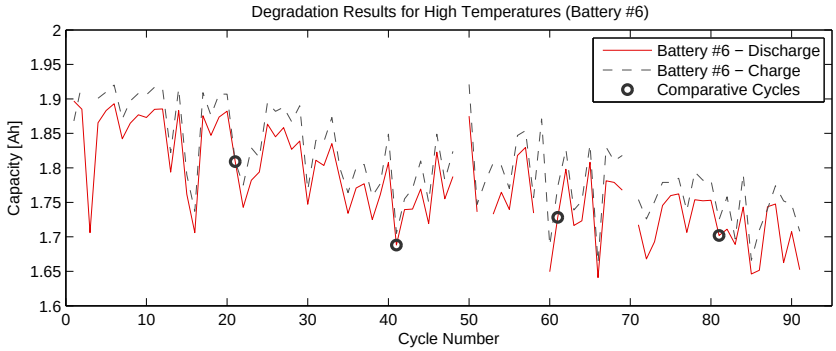

Figure 3.12: Degradation data obtained discharging Battery #6 at high temperature.

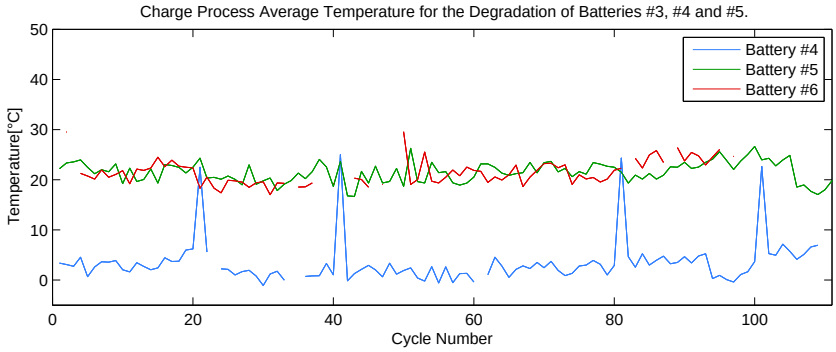

Figure 3.13: Average temperature of the charge process for each cycle of the degradation data.

3.2 Battery Temperature Dependence Results

In addition to the degradation data, some test are conducted to study the behavior of the cells at different temperatures. The objective is to establish a relation between the capacity of the battery and the ambient temperature, and an expression for the approximated internal impedance as a function of the battery's temperature.
The Battery #3 was used to realize the experiments of this section. This battery was obtained from the same pack than the batteries used for the degradation tests.

3.2.1 Battery Capacity as a Function of the Temperature

To obtain the battery capacity dependence on the temperature, the battery is fully charged with the same protocol as the presented for the accelerated degradation data set, and then discharged until a cut-off voltage of $0.5[V]$, using the load profile shown in Figure 3.14. This profile corresponds to a constant current at nominal values ($2.4[A]$), in addition to a pair of two pulses placed inside a range of SOC of 80% and 20%. For this range of SOC values, the internal impedance remains approximately constant [55]. Using the information of the charging process, the time location of the pulses can be readjusted to ensure that they are placed inside the desired SOC range.

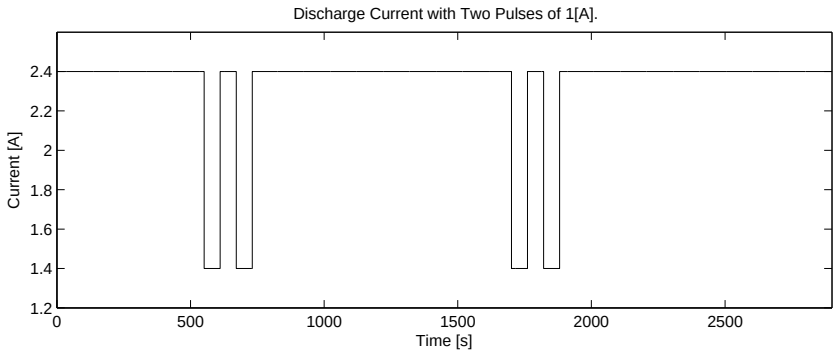

Figure 3.14: Load profile consisting of a constant current of $2.4[A]$, and pulses of $\Delta I = 1[A]$.

The cell's delivered capacity is obtained by integrating the current over time for each cycle independently. Figure 3.15 shows the charge capacity as a function of the ambient temperature of the charge process.

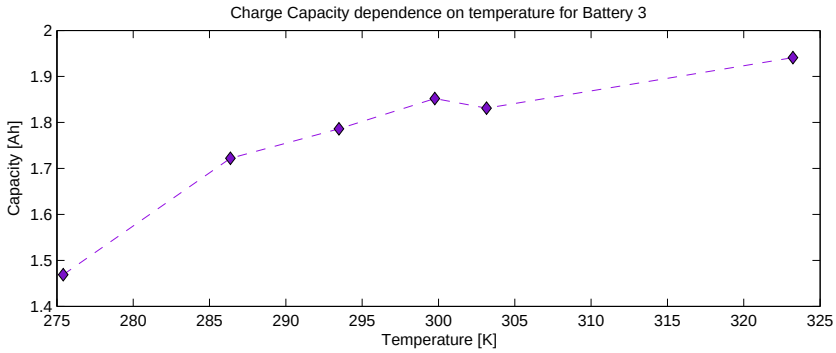

Figure 3.15: Charge capacity dependence on temperature for Battery #3. Each diamond corresponds to a cycle result.

3.2.2 Temperature Dependence of Internal Impedance

In order to obtain an estimation of the internal impedance, given by $|\frac{\Delta V}{\Delta I}|$, it is necessary to compensate the voltage drop associated to the battery discharge ΔV_{SOC}. Figure 3.16(a)

illustrates the battery voltage and ΔV_{SOC} for a current profile presented in Figure 3.16(b), where the difference between current levels is ΔI. The internal impedance estimate is expressed in Equation (3.1).

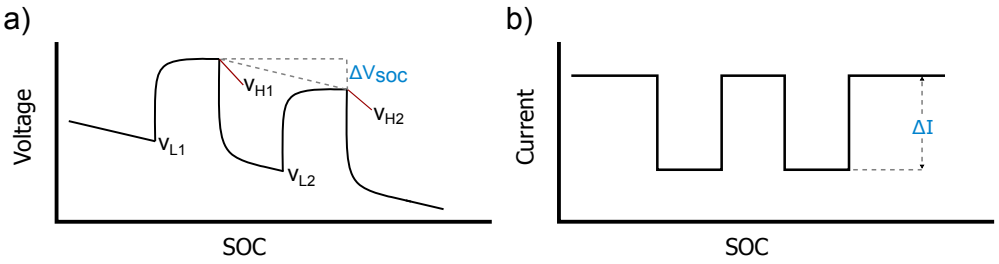

Figure 3.16: (a) Illustration of the changes on the battery voltage due to current changes between two values. (b) Discharge current consisting of a constant current and two pulses.

$$|Z_{int}| \approx \left| \frac{V_{H1} - V_{L2} - \frac{\Delta V_{SOC}}{2}}{\Delta I} \right| \tag{3.1}$$

$$\approx \left| \frac{V_{H1} - V_{L2} - \frac{1}{4}\left(V_{L1} - V_{L2} + V_{H1} - V_{H2}\right)}{\Delta I} \right| \tag{3.2}$$

This approximation represents the information of the battery's internal impedance on the linear zone for the frequencies contained in the pulses and not the complete frequency spectrum, as the results obtained using the EIS test. However, this method can be used on-line, and approximation errors can be neglected depending on the applications.

The cell's impedance depends on the temperature, and for each temperature value, a different estimation of $|Z_{int}|$ is calculated.

To obtain the approximation expressed in (3.1), the Battery #3 was discharged to a high DOD value, and then fully charged. After that, the cell was discharged until the integration of the current obtained from the battery was approximately a 25% of the charge capacity (obtained integrating the charge current). Then, for five different values of the ambient temperature, two current pulses between 2.4[A] and 1.4[A] were applied to the battery (see Figure 3.16.b). After these pulses, the battery was charged trying to mantain the SOC around a 75%, charging the same capacity value as the drained from the battery during the two pulses discharge. The result for the estimation of the internal impedance as a function of the temperature is shown in the Figure 3.17. This experiment shows a clearly dependence of the absolute value of the internal impedance on the battery temperature, with a lower impedance for higher temperatures. The results are consistent with the Nyquist plots of the internal impedance of the Figure 2.8

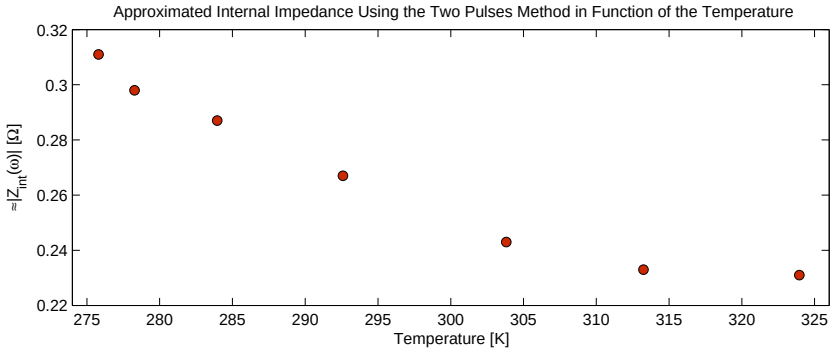

Figure 3.17: Approximation of the cell internal impedance for different temperatures.

3.3 Data Available at Public Databases

Apart from the generated data, there is also available accelerated degradation data of 36 Li-Ion cells provided by the Prognostics Center of Excellence at NASA Ames [56]. Figure 3.18.a) presents the degradation results of a cell cycled at an ambient temperature of $296.15[K]$, using a constant discharge current of $2[A]$. The results showed in Figure 3.18.b) correspond to the degradation of a cell operated with the same conditions of the first one, but with an ambient temperature of $277.15[K]$. Both cells have a nominal capacity of $2[Ah]$.

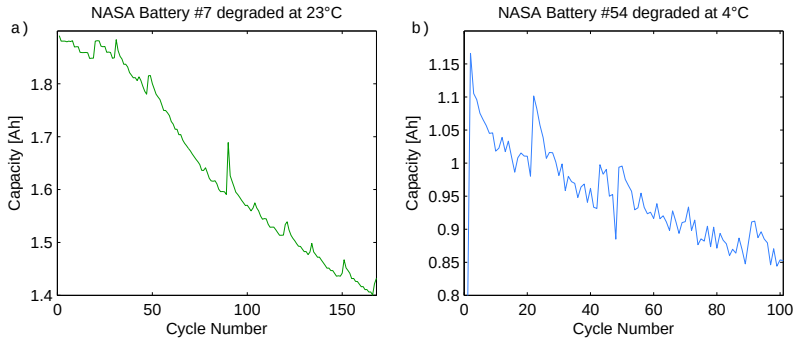

Figure 3.18: Example of accelerated degradation data provided by NASA Ames Prognostics Center of Excellence.

Chapter 4

Particle-Filtering-based Scheme for State-of-Health Prognosis at a Reference Temperature

This chapter presents the proposed solution for the SOH estimation and RUL predictions of Li-Ion batteries within a particle-filtering-based framework. The main topics include the proposed state-space model for battery degradation with the inclusion of the temperature of operation, the issues related to the implementation of the particle filter algorithm, and the results of the SOH prognosis. This framework is validated using the degradation data depicted in Chapter 3, in addition to an artificial data set generated to test the performance of the proposed scheme.

4.1 Model Proposal for a SOH Prognosis Scheme at a Reference Temperature

Modeling the degradation of an ESD is a complex task, since the amount of variables involved on battery aging and their interaction (see Section 2.1.1). An electrochemical approach may result in a better model than other simplified options, but increasing the computational complexity of the final algorithm and the efforts to obtain the value of the model parameters (see Section 2.2.2). This difficulty is given mainly by the existence of parameters that depends on (i) operational conditions as the magnitude of the current drained from the battery or the ambient temperature, and (ii) the chemistry of the electrodes and the electrolyte. As a consequence, this work proposes a model to describe the evolution of the degradation of a Li-Ion battery with an empirical state-space non-linear model, based on the work of Olivares *et al.* in [43], [57], instead of an electrochemical approach. That base model was developed and tested within a Bayesian-filtering scheme with satisfactory results, but an important factor is assumed constant: The temperature.

The purpose and contribution of this work is to estimate and predict the SOH of a Li-Ion battery, considering its temperature of operation. The explicit inclusion of that variable in the model is needed due to its importance on the energy that a battery can store and deliver (see Section 2.1.3). The neglection of this input variable may lead to wrong decisions if these are based solely on the observed capacity for the current cycle.

Equations (4.2) - (4.5) show the proposed state-space dynamic model to achieve the SOH estimation and prognosis. The inputs of the model corresponds to the average temperature $T[K]$ during the charge process on the cycle k (assuming the same average temperature for the charge and discharge processes), and the output of a self-regeneration phenomena detection module $U(k)$. The model output is the measured capacity of the battery during the k^{th} cycle at the temperature of operation $T(k)$. η is an efficiency parameter that explains how much energy is expected for a cycle given the delivered in the previous one.

The state $x_1(k)$ is associated to the SOH (or degradation) of the battery at the reference temperature T_{ref}. State $x_2(k)$ is an unknown parameter required to explain differences between the actual degradation trend with respect to the expected for x_1, under the concept of artificial evolution [35]. The state $x_3(k)$ is associated with the additional available energy due to regeneration phenomena and allows the inclusion of that extra capacity only in the observation equation and not in x_1. Function $\delta(\cdot)$ corresponds to the Kronecker delta,

$$\delta(U) = \begin{cases} 0, & \text{if } U \neq 0 \\ 1, & \text{if } U = 0. \end{cases} \tag{4.1}$$

Process noises ω_1 and ω_2, and observation noise v are zero-mean Gaussian noise terms; ω_{31} is a log-normal noise used to characterize the typical amount of SOH that is added in the event of successive regeneration phenomena; ω_{32} is used to characterize the typical damping ratio of self-recharge phenomena and distributes as a Uniform over the range [0.75, 0.85]. Both $\omega_{31}(k)$ and $\omega_{32}(k)$ were determined statistically in [43] studying the accelerated degradation data provided by NASA Ames Porgnostic Center of Excellence.

State-of-Health Dynamic Model

State transition equations:

$$x_1(k+1) = x_1(k)(\eta + x_2(k)) + \omega_1(k) \cdot \phi(T(k)) \tag{4.2}$$
$$x_2(k+1) = x_2(k) + \omega_2(k) \tag{4.3}$$
$$x_3(k+1) = \delta(U(k))\omega_{31}(k) + \delta(1 - U(k))(x_3(k)\omega_{32}(k)) + ... \tag{4.4}$$
$$... + \delta(2 - U(k))(x_3(k) + \omega_{31}(k))$$

Measurement equation:

$$y(k) = C_{use}(x_1(k), T(k)) + (\delta(1 - U(k)) + \delta(2 - U(k))) \cdot x_3(k) + v(k) \tag{4.5}$$

For the purposes of this work, the battery capacity $C(k)$ in the cycle k is approximated by the Coulomb counting method, using the current data $i_k(t)$ of the discharge process in the

k^{th} cycle. That is to say, $C(k) = \int \mathrm{i}_k(t)\mathrm{d}t \approx \sum_j \mathrm{i}_k(j)\Delta t$, being Δt the sample time of the sensors for the discharge process. Furthermore, the state $x_1(k)$ does not correspond directly to the SOH, but to a capacity measure (in $[Ah]$) in order to easily establish the observation equation. To obtain a true value of the SOH (by the common definition in percentage) it is necessary to divide the state x_1 by the nominal capacity of the battery, or in the absence of this value by the capacity delivered at the first cycle of operation (assuming in a valid first measurement).

4.1.1 Inclusion of the Temperature of Operation of the Battery

One of the goals of the proposed degradation model is to provide a state $x_1(k)$ that can be related directly to the battery SOH, at a reference temperature. Measurement equation (4.5) represents the measured capacity $y(k)$ by the sum of a function of the state $x_1(k)$, a term that depends on the state $x_3(k)$, and the observation noise $v(k)$. In this regard, this section focuses on the explanation of the term $C_{use}(x_1(k), T(k))$. This function of $x_1(k)$ intends to include the temperature of operation by the concept of *Usable Capacity*, corresponding to the expected amount of capacity that the battery can deliver or store in the k^{th} cycle at a given SOH and average temperature $T(k)$. The evolution of the state associated to the SOH should be described by

$$C_{use}(x_1(k+1), T(k)) = C_{use}(x_1(k), T(k)) \cdot (\eta(T(k)) + x_2(k)) + \omega_1(k), \tag{4.6}$$

with C_{use} a function that lets one to establish a comparison of the actual SOH at different values of T. Under the assumption that the battery is working within a temperature range where the operation temperature does not change the tendency of degradation in just a few cycles, $\eta(T(k))$ can be considered as a constant η (the uncertainty induced by the latter is included in x_2 due to its artificial evolution). Figure 2.5 shows an "ideal working temperature range" where the batteries EOL are similar, providing a prior knowledge about the temperature values that satisfies this assumption. Furthermore, the laboratory generated data, shown in Section 3.1.2, presents similar degradation trends for the three cells. Their comparative cycles at room temperature (21^{st}, 41^{st}, 61^{st}, 81^{st} and 101^{st} cycles) show a similar degradation.

The relation between the delivered capacity and the average temperature in a cycle can be established with the equation (4.7) of Vogel-Tammann-Fulcher (VTF) suggested in [45]. In that relation $C^{SOH}_{T_{ref}}$ is the capacity that the ESD delivers in its actual SOH at a reference temperature T_{ref}, and α and β are parameters that have to be fitted to capacity versus temperature data. If the state x_1 is defined as $C^{SOH}_{T_{ref}}$, then (4.7) becomes (4.8). This function was fitted to the data presented in Section 3.2.1, and is shown in Figure 4.1. The results are $\alpha = -5.1593$ and $\beta = 260.9565$, with a mean-squared error of 2.1721×10^{-4}.

$$C_{use}(C^{SOH}_{T_{ref}}, T) = C^{SOH}_{T_{ref}} \cdot \mathrm{e}^{\alpha\left(\frac{1}{T-\beta} - \frac{1}{T_{ref}-\beta}\right)} \tag{4.7}$$

$$C_{use}(x_1, T) = x_1 \cdot \mathrm{e}^{\alpha\left(\frac{1}{T-\beta} - \frac{1}{T_{ref}-\beta}\right)} \tag{4.8}$$

Using (4.8) in (4.6), and dividing by the exponential term,

$$x_1(k+1) \;=\; x_1(k)(\eta + x_2(k)) + \omega_1(k) \cdot \mathrm{e}^{\overbrace{-\alpha\left(\frac{1}{T(k)-\beta}-\frac{1}{T_{ref}-\beta}\right)}^{\phi(T(k))}}, \tag{4.9}$$

an equation that describes the evolution of the state x_1 at a fixed reference temperature T_{ref} is found, being the same as (4.2).

An important assumption made for this work is that this adjustment is invariant with cycling and time, but as the internal impedance increase with a lower SOH, it may be expected that the values of α and β change when the battery has degraded. In this regard, a complete study of the batteries should include characterization of this relation for several different states of degradation.

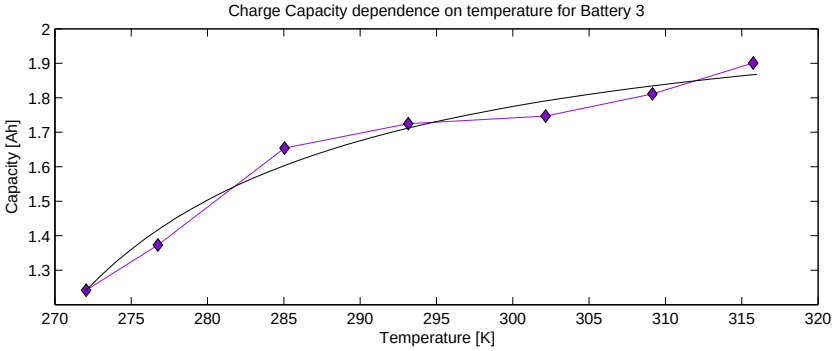

Figure 4.1: VTF curve adjustment to data of capacity delivered by a cell in a complete cycle at different temperatures.

4.1.2 Regeneration Phenomena Detection Module

One of the inputs of the system described by the equations (4.2)-(4.5), $U(k)$, is defined as the output of an online PF-based detection module developed in [43]. This module performs a hypothesis test with a 1% of false alarm rate for the measurement $y(k)$, considering the *a priori* prediction of the system output as the pdf that characterizes the null hypothesis (self-recharge phenomena either do not exist or are fading in time). To achieve this task, the detection module determines a time-varying threshold that depends on the position of the particles associated to the empirical *a priori* state distribution. The possible values for $U(k)$ are presented in (4.10).

$$U(k) = \begin{cases} 0 & \text{if self-recharge does not exist,} \\ 1 & \text{if either self-recharge is detected at cycle } k \\ & \text{or self-recharge phenomenon is fading,} \\ 2 & \text{if additional self-recharge phenomena are} \\ & \text{detected before the latest one fades.} \end{cases} \tag{4.10}$$

Figure 4.2 illustrates the PF-based detection framework for self-recharge phenomena for five regeneration events, where Figure 4.2.a shows degradation data, Figure 4.2.b the output of the PF-based detection module (*detection signal*), and Figure 4.2.c the external input $U(k)$ generated according to (4.10).

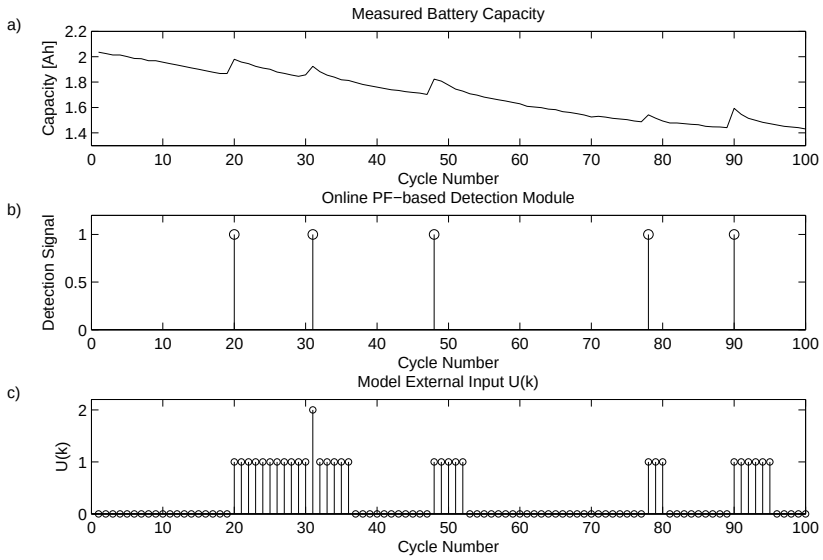

Figure 4.2: Illustration of the PF-based detection framework for self-recharge phenomena.

This module was developed to operate with the measured capacity and the state x_1. However, it cannot be directly applied to temperature-varying data. The development of a model that has a state x_1 that represents the SOH at a reference temperature allows the use of this detection module if the comparisons are made between x_1 and the transformation of the measured capacity $y(k)$ to a reference temperature $y_{Tref}(k)$, by using (4.7).

$$y_{Tref}(k) \quad = \quad y(k) \cdot \mathrm{e}^{-\alpha\left(\frac{1}{T-\beta}-\frac{1}{T_{ref}-\beta}\right)} \tag{4.11}$$

4.1.3 Outer Feedback Correction Loop for Erroneous State Initialization

From the perspective of the implementation of the SOH prognosis scheme in a real application, the algorithm needs to be robust and work outside ideal conditions. The initial state value of an ESD (in particular $x_1(k=0)$) may be unknown, or even it may be erroneous if a nominal value is used for a low quality or cheap battery. In those cases, the scheme must be able to correct an erroneous initialization of the state x_1 and converge rapidly to a reasonable value. An easy approach to solve this issue is to use the observation data of the first cycle and initialize the state x_1 with that value, but nothing assures that it is not an erroneous value or an outlier. In this regard, an outer-loop correction is proposed to deal with this problem.

The core idea of this outer feedback correction loop is to modify the process noise ω_1 in order to explore a wider range of values with the particles $x_1^{(i)}$ during the first iterations of the PF algorithm. To achieve this task, the implementation of this procedure considers starting the PF algorithm with a boolean variable `errorCI` initialized with the value 1. While `errorCI` is equal to 1, the output of the regeneration detection module is $U = 0$ and the process noise ω_1 depends on the difference between the measurement and $C_{use}(x_1, T)$. Once the aforementioned difference is less than a threshold (that could be a percentage of the nominal capacity of the ESD), `errorCI` becomes 0 and the regeneration detection module starts to work. It is worth to mention that this outer-loop is only active during the beginning of the filtering stage, and once `errorCI` changes from 1 to 0 it will never be active again. A summary of the explained procedure is presented as a pseudo-code.

Pseudo-algorithm of erroneous initial condition outer feedback correction loop.

procedure ESTIMATION($\cdot$)
  $errorCI \leftarrow 1$
  while $k < k_{prognosis}$ **do**
    $\mathbf{e} \leftarrow C_{truth}(k) - y(k)$
    if $(\sim errorCI)$ **then** ▷ Working Detection Module
      U(k) $\leftarrow$ REGENERATION_DETECTION_MODULE($\cdot$)
    else$(errorCI)$ ▷ Process noise of x_1 is modified
      U(k) $= 0$
      $\sigma_{\omega_1} = 0,0042 + 1,05 \cdot \langle w_k^{(i)}, |\ \mathbf{e}\ | \rangle$
      if $\langle w_k^{(i)}, |\ \mathbf{e}\ | \rangle < e_{th}$ **then**
        $errorCI \leftarrow 0$
        $\sigma_{\omega_1} = 0,0042$
      end if
    end if
    PF_FILTERING( ) ▷ One iteration of the filtering stage
  end while
end procedure

In this pseudo-code, k corresponds to the k^{th} cycle of operation of the ESD, $k_{prognosis}$ represents the cycle where the prognosis procedure starts, $C_{truth}(k)$ is the measurement capacity of the battery, $y(k)$ is the output of the dynamic degradation model, and $w_k^{(i)}$ the weights of the PF algorithm.
The presented pseudo-algorithm shows stages of the PF algorithm and the regeneration detection module. Nevertheless, this procedure only modifies the value of the process noise ω_1 of the state-space model.

4.2 Issues Related to the Implementation of the SOH Prognosis Scheme

As discussed in Section 2.2.2, particle filtering algorithms are a suitable option to work with non-linear and non-necessarily Gaussian models, and to represent the uncertainty of the system in the prognosis stage. In this regard, the SOH prognosis is achieved with a particle-filtering-based scheme using the model of the equations (4.2) - (4.5). The Sequential Importance Sampling algorithm (see section 2.3.2) is used for the estimation stage, and the prognosis algorithm corresponds to the approach based on the regularized particle filter (see Section 2.3.3), applying the regularization to the states x_1 and x_2. The following sections are concerned to the PF algorithm implementation.

4.2.1 Configuration of the Particle Filter Algorithm

The formulation of PF-based prognostic approaches has been widely covered in literature [28], [35], [33]. However, there are specific issues associated to the implementation of these schemes that depend, in a strong manner, on the number of states of the dynamic system and the type of non-linearities exhibited by them. In order to determine the value of those parameters for the SOH prognosis scheme with the proposed model of the equations (4.2) - (4.5), it is required to compare the performance of this suboptimal scheme with respect to an analytic solution; a complex task given the non-linearities of the considered model. For this reason, a reasonable method to set the filter parameters is the one adopted by Olivares *et al.* in [43], where a simplified scenario is used to determine an adequate configuration of the PF algorithm by using a linear Gaussian dynamic system. With this methodology the performance of the proposed PF-based SOH prognosis framework is compared versus the optimal solution given by the *a priori* prediction equations of the Kalman filter. As the model proposed in this work is generated from the one used in [43], it is considered that those results are appropriate for this work. The configuration is: (i) 50 particles, (ii) 40 realizations of the non-linear filter, and (iii) 50 realizations of the long-term predictions. The value of 50 particles is the lower amount that presents a similar result as the analytic solution. Thus, an increment in the number of particles does not affect the performance of the scheme. To facilitate the calculation of confidence intervals of 95% and integer percentage values of a resulting *a posteriori* distribution (e.g. 99%), the number of particles is duplicated to 100. With that number, the execution of the SOH estimation and prognosis procedures takes less than 1.5[sec] using the MATLAB® environment and a Intel® Core$^{(TM)}$ i7 CPU (3.07GHz) and 16GB of RAM.

4.2.2 Dealing with Outliers and Loss Data

Observing the generated degradation data presented in Section 3.1.2 it is easy to see outliers in the measured capacity data (with an abrupt capacity loss for just one cycle) that may

affect the performance of the filtering stage and result in a wrong assumption of a degraded battery. Moreover, there are some cycles where capacity or temperature data is not available. The approach used to operate with this type of data is to execute the prognosis stage while data is missing or is considered as an outlier; by using the previous cycle number as the prediction time and the corresponding value of the state vector to begin the prediction. At the time instant when new data is valid and available (measured capacity and temperature of operation of the cycle), the filtering stage restarts with the state value of the last prediction time instant. A more appropriate method should consider an imputation algorithm [58] within the PF to incorporate the available knowledge for the required cycle.

Figure 4.3 illustrates this procedure for an example with the state-space equations:

$$x_{k+1} = \eta \cdot x_k + w, \tag{4.12}$$

$$y_k = x_k + \nu, \tag{4.13}$$

where data is not available from cycles τ to $\tau + 5$ ($\eta < 1$). The estimator $\hat{x}_k$ can be obtained for $k = 0, ..., \tau - 1$, and the prognosis stage starts at $k = \tau$, obtaining the prediction $\hat{x}^*_k$. When a new measurement is valid, for $k = \tau + 6$, the estimation of $x_{\tau+6}$ uses the predicted value for $\tau + 5$ and its weight vector, that is $\hat{x}_{\tau+5} = \hat{x}^*_{\tau+5}$ and $\omega^{(\mathrm{i})}_{\tau+5} = N^{-1}$.

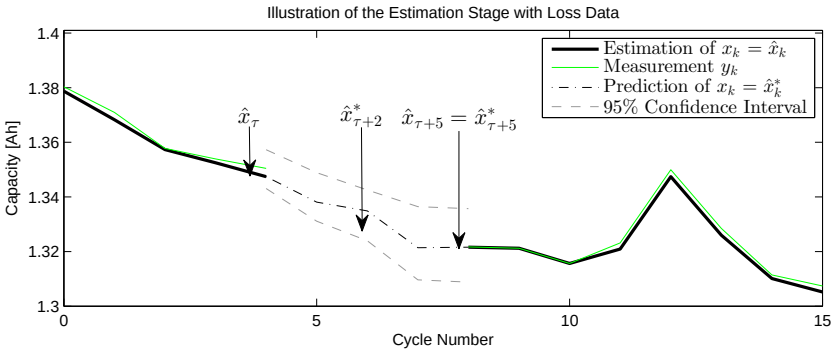

Figure 4.3: Illustration of the procedure to estimate a state x in presence of missing data. Thin green line is the measurement $y(k)$, dark bold line corresponds to the estimator $\hat{x}_k$, dash-dotted line is the prediction $\hat{x}^*_k$, and gray dashed lines are the prediction confidence interval.

To determine whether a new measurement is an outlier or not, a hypothesis test is applied to compare the *a priori* observation equation with respect to the measured capacity, both transformed to a value at a reference temperature according to (4.7). The null hypothesis H_0, corresponding to a new measurement that is valid, is characterized by the *a priori* one-step-ahead prediction of the system output PDF. The false alarm probability (p_{fa}) is set to 1%. This test uses a time-varying threshold $\Theta_{th}(k)$ that depends on the position of the state particles, defined as the difference between a scalar $\Theta_y(k)$ and a constant K_{th} (a 12% of the nominal capacity). The scalar is obtained from the particles that satisfies $\Sigma\omega^{(\mathrm{i})}(k) > p_{fa}$ and $h(x^{(\mathrm{i})}(k)) > \Theta_y(k)$ (being $h(x)$ the measurement equation (4.5)), resulting in $\Theta_{th}(k) = \Theta_y(k) - K_{th}$. That is, the null hypothesis is rejected if the measurements are a fixed amount below most of the particles' position. This test is illustrated in Figure 4.4 for a continuous PDF and p_{fa} of α%.

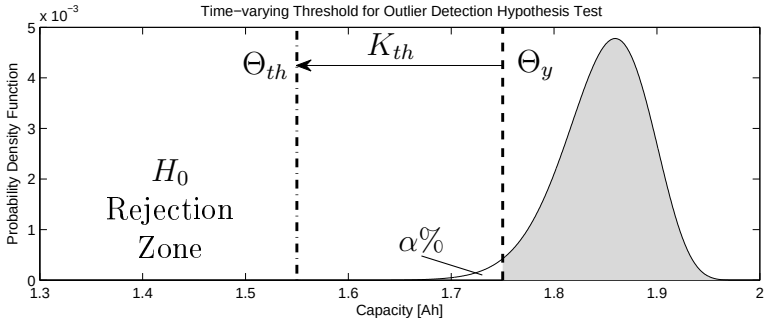

Figure 4.4: Illustration of the PF-based hypothesis test for outlier detection.

4.2.3 Validation Data

Data presented in Section 3 show the degradation of Li-Ion cells, being each cell operated approximately at the same temperature for every cycle (excluding the comparative cycles added in the laboratory generated data). That data is, however, not enough to completely validate the proposed SOH prognosis scheme. It is necessary to count with degradation data where a battery has different temperatures of operation for different cycles. To evaluate the capability of the scheme to work in these conditions, an artificial data set was made from the degradation data of a battery available at NASA Ames repository [56]. The use of the artificially generated data is to test the performance of the scheme, and does not imply a proof of the assumption of similar degradation trends for a given temperature range.

The SOH estimation and prognosis scheme requires, for each cycle, the average temperature of operation, the measured capacity, and the parameters α and β that satisfies (4.7). With those values, a capacity at a reference temperature T_{ref} can be obtained. To generate an artificial data set, the process is reversed using the values of α and β obtained for the cells tested in the laboratory. Then, creating an arbitrary temperature set with values fluctuating between $275[K]$ and $298[K]$, a capacity measurement is made using the transformation (4.7) over capacity data at $298[K]$. A random noise is added to the new capacity measurements to include uncertainty associated to the characterization of (4.7). Accelerated degradation data presented in Figure 3.18.a (provided by NASA Ames Prognosis Center of Excellence) is selected to generate the artificial data set. Figure 4.5.a shows the resulting generated capacity measurement at the temperature shown in Figure 4.5.b.

Four degradation data sets are considered for the scheme validation, and are referred to as DS #1, #2, #3, and #4. They correspond to:

- **DS #1:** NASA Ames accelerated degradation data at $23[^oC]$. Capacity data is intentionally deleted for cycles 19 to 23 and replaced by $1.3[Ah]$ for cycles 60 to 62 to test the outlier detection module.
- **DS #2:** Degradation results for Battery #4 ($\approx 23[^oC]$).
- **DS #3:** Degradation results for Battery #5 ($\approx 3[^oC]$).
- **DS #3:** Artificially generated degradation at different temperatures of operation.

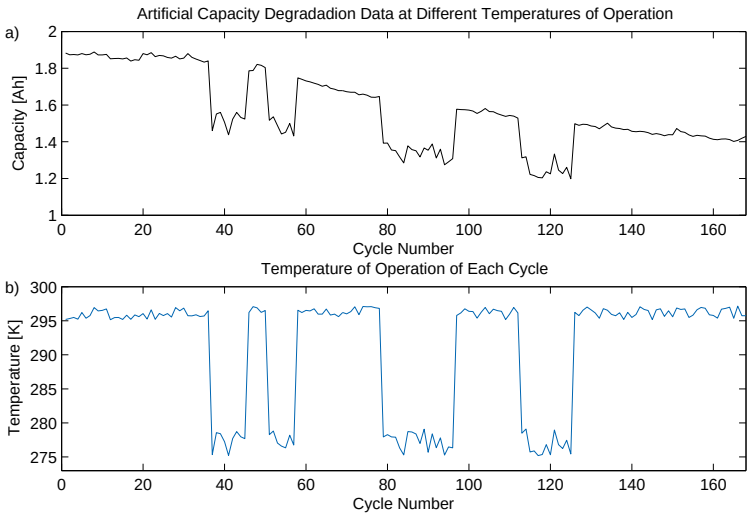

Figure 4.5: Artificially generated degradation data.

4.3 Validation of the SOH Prognosis Module

The principal purpose of the state-space model presented in (4.2)-(4.5) is working the degradation data at a reference temperature (T_{ref}). Therefore, the long-term predictions of the state vector are conducted at T_{ref} using the results of the filtering stage as the initial condition. Then, equation (2.49) can be used to obtain a probabilistic characterization of the EOL of the battery, by finding the time instants where each particle trajectory (at T_{ref}) reaches a given percentage of capacity loss. Figures presented in this chapter illustrate the performance of the SOH PF-based prognosis scheme for one realization of the non-linear filter, and one realization of the long-term prediction.

Figures 4.6, 4.7 and 4.8 present the results of one realization of the prognosis scheme for DS#1. The initial condition of the particles of x_1 are set around $1[Ah]$ (half the nominal capacity), and some cycles were deleted while others were changed for a lower value to test the outlier detection module. Figure 4.6 shows the validation data (bold black line), state x_1 estimation (orange line), the observation of the model (dashed green line), and long-term predictions (dashed bold blue line). All of them are presented at a reference temperature of $23[^oC]$. In addition, red circles show the cycles where the detection signal of the regeneration phenomena detection module is non-null. Gray lines correspond to predictions of the particles of the state x_1, and segmented magenta lines represent the confidence interval of 95%. This result illustrates how the outer feedback correction loop allows x_1 to converge to a reasonable value given the observations, and allows the scheme to work properly even with an erroneous initialization of x_1. The prediction instant is the 107^{th} cycle (dark vertical segmented line), but some predictions can be seen between cycles 19 to 23 and 60 to 62 due to the outlier detection module. The latter is important when working with non-ideal data. The evolution of x_2 is presented in Figure 4.7, exhibiting predictions of the state vector during the filtering stage (as in Figure 4.6). Figure 4.8 shows the evolution of x_3 ($x_3(k) = 0;\ k > k_{predict}$), that explains the difference between the observation equation and x_1 during the filtering stage; in

addition to the detection signal (represented by red circles in Figure 4.6). In this experiment in particular, the failure threshold was diminished to a 65% of the nominal capacity to illustrate in a better manner the proposed scheme (to include an erroneous initialization, more regeneration phenomena, and lost data). With this consideration, the ground truth EOL is 143, and the expected EOL is 147 for a 40-cycle prediction window. However, this example is just one illustrative realization of the SOH prognosis scheme.

An evaluation of the inclusion of the regularization approach for the SOH prognosis was made using the results presented in Figure 4.6. The higher uncertainty introduced by the regularization algorithm (see Figure 4.9) reduces the accuracy of the prognosis, even resulting in particles that do not cross the hazard zone. However, it helps to include the future uncertainty involved in battery degradation.

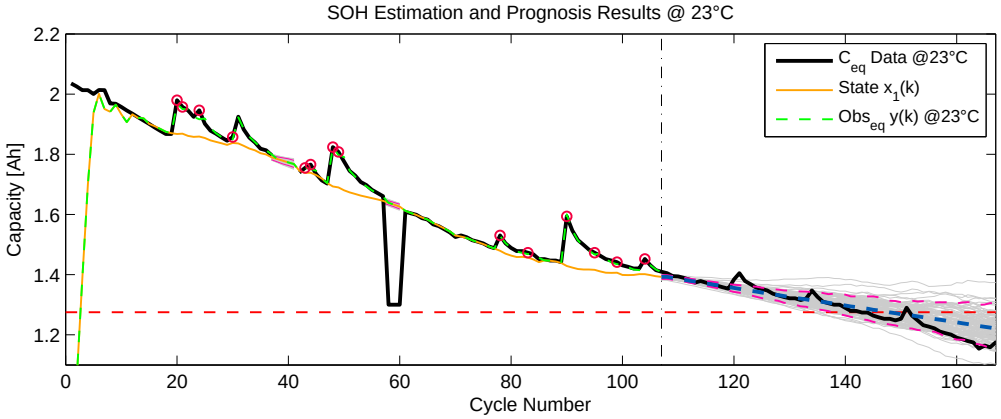

Figure 4.6: SOH prognosis for DS#1 using the proposed PF-based framework. Degradation data (bold black line), estimated x_1 (orange line), model observation y (segmented green line), predicted x_1 (bold blue dashed line), and 95% confidence interval for x_1 prediction (thin segmented magenta line); all at a reference temperature of $23[^oC]$.

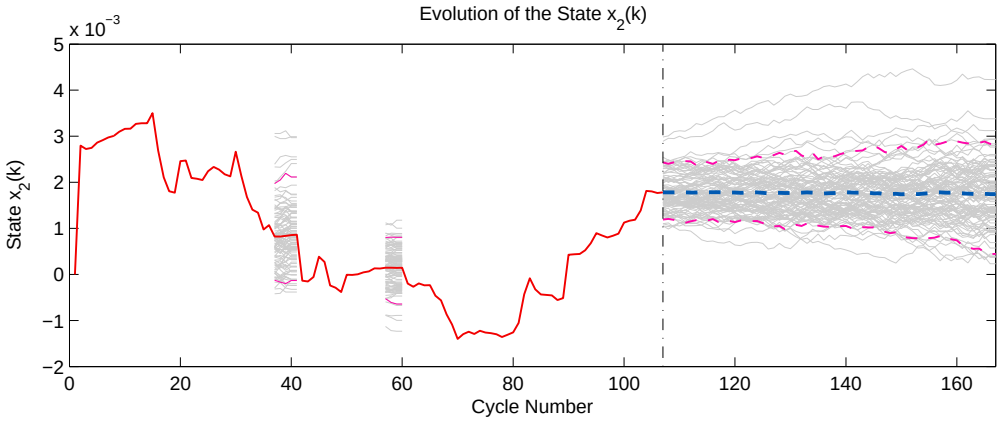

Figure 4.7: Evolution of the state x_2 for DS#1 using the proposed PF-based framework. Estimated x_2 (red line), predicted x_2 (bold blue dashed line), and 95% confidence interval for x_1 prediction (thin segmented magenta line).

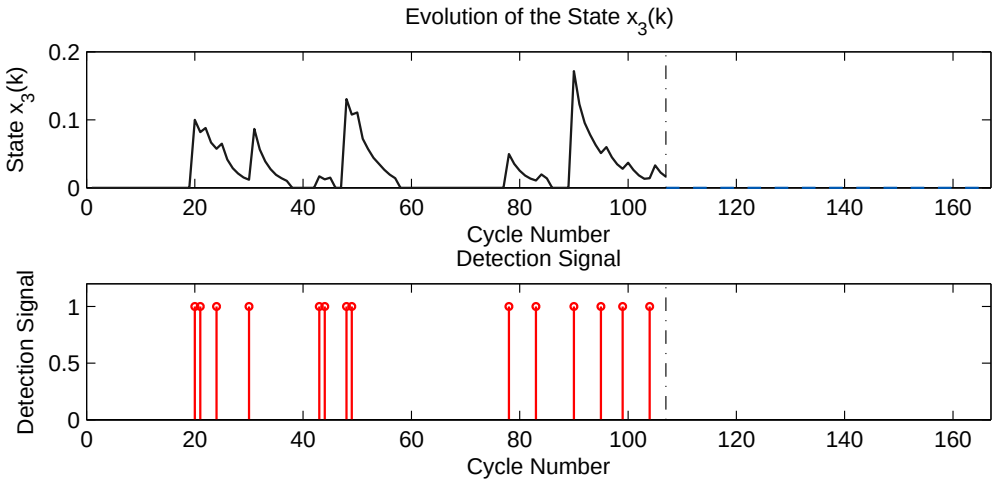

Figure 4.8: Evolution of the state x_3 and the Detection Signal for DS#1 using the proposed PF-based framework.

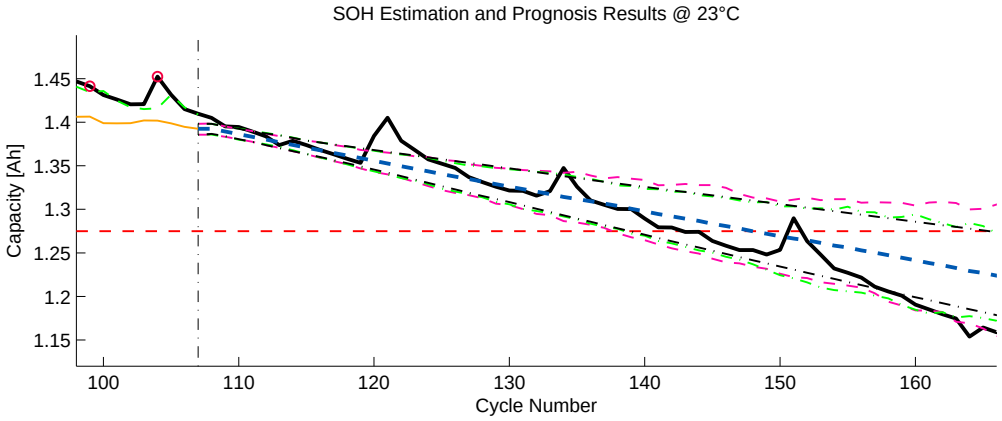

Figure 4.9: Influence of the regularization algorithm in the prognosis stage for DS#1. Degradation data (bold black line), estimated x_1 (orange line), model observation y (segmented green line), predicted x_1 (bold blue dashed line), prediction instant (black dot-dashed line), 95% confidence interval for x_1 prediction with regularization for x_1 and x_2 (thin segmented magenta line), 95% confidence interval for x_1 prediction with regularization for only x_1 (thin dot-dashed black line), and 95% confidence interval for x_1 prediction without regularization (thin dot-dashed green line).

Figures 4.10 and 4.11 show the evolution of x_1, the observation, and the measurement data (analogous to the Figure 4.6) for the laboratory generated degradation DS#2 and DS#3 respectively. For those noisy sets, the self-regeneration detection module not only works with its original purpose, but also for high capacity peaks that last one or two cycles, making the SOH evolve smoothly as it would be expected. From the perspective of a risk-based decision, it is not critical to have the regeneration detection module working in that manner, because it may result in an underestimation of the SOH most of the time. The noisy behavior of these data set makes difficult to establish the time instant of the ground truth EOL, but for DS#2 the predictions can be compared with data post cycle 85. To evaluate the long-term predictions of x_1 the ground truth EOL value can be set at $1.598[Ah]$ at cycle 95. The expectation of $\hat{x}_1^*$ crosses the EOL threshold at the 104^{th} cycle.

The results of the long-term predictions of x_1 for the artificial degradation set DS#3 are presented Figure 4.12. This data set is used to evaluate the operation of the proposed scheme with a time varying temperature of operation. However, an experimental degradation data set -with different temperatures- is required to validate the scheme. As one may observe, the scheme produces both the estimations and predictions of the state x_1 at a reference temperature, allowing the application of the outer-feedback correction loop and the self-regeneration detection module over temperature varying degradation data.

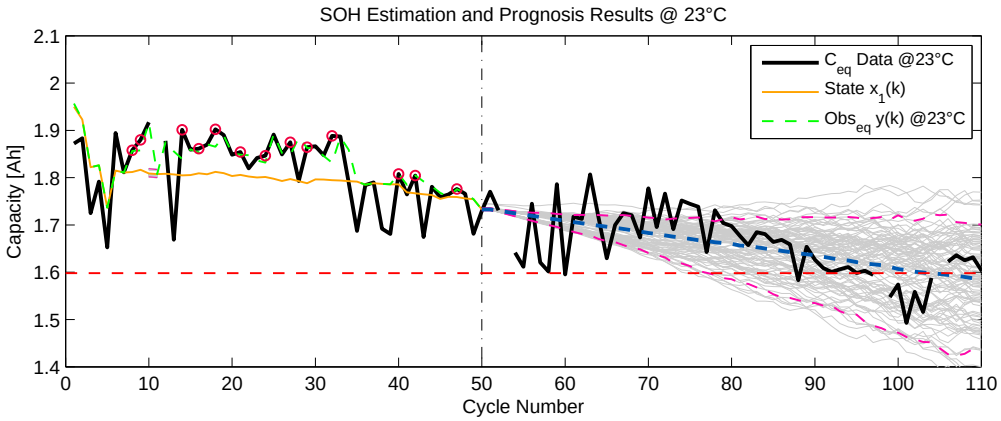

Figure 4.10: SOH prognosis for DS#2 using the proposed PF-based framework. Degradation data (bold black line), estimated x_1 (orange line), model observation y (segmented green line), predicted x_1 (bold blue dashed line), and 95% confidence interval for x_1 prediction (thin segmented magenta line); all at a reference temperature of $23[^oC]$.

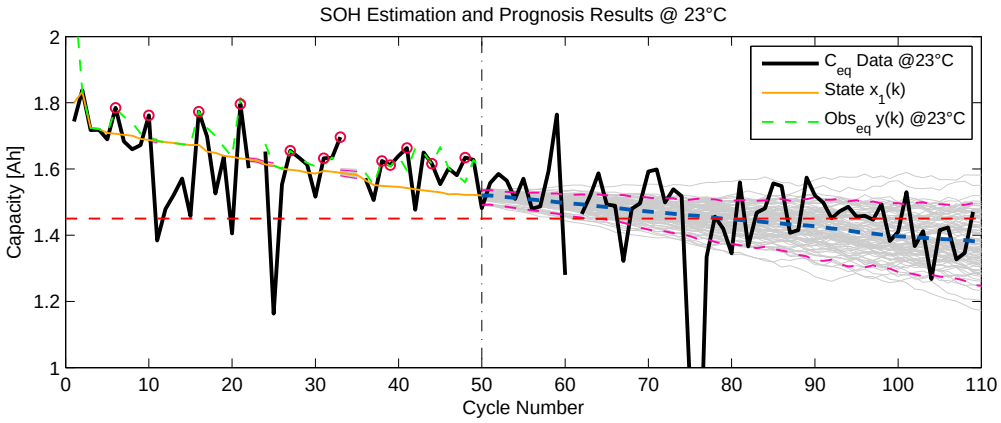

Figure 4.11: SOH prognosis for DS#3 using the proposed PF-based framework. Degradation data (bold black line), estimated x_1 (orange line), model observation y (segmented green line), predicted x_1 (bold blue dashed line), and 95% confidence interval for x_1 prediction (thin segmented magenta line); all at a reference temperature of $23[^oC]$.

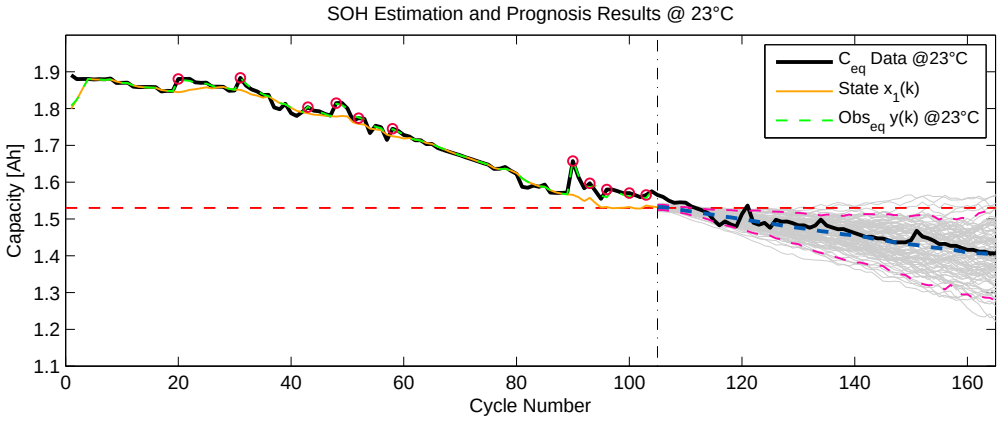

Figure 4.12: SOH prognosis for DS#4 using the proposed PF-based framework. Degradation data (bold black line), estimated x_1 (orange line), model observation y (segmented green line), predicted x_1 (bold blue dashed line), and 95% confidence interval for x_1 prediction (thin segmented magenta line); all at a reference temperature of $23[^oC]$.

4.4 Final Remarks of This Section

This work proposes a detailed method to include the temperature of operation of the batteries within a probabilistic SOH prognosis scheme, in contrast with previously developed schemes that considers a constant temperature. The incorporation of the "Usable Capacity" allows the inclusion of the impact of the temperature, and may be a suitable option to include the effect of DOD. Both variables must be considered for any battery degradation monitoring system in real applications. However, additional battery degradation data is required to validate and also to improve this scheme.

A side result of this work is the understanding of the type of degradation tests that are required for the sintonization and implementation of temperature-dependent models. This point is important for the generation of degradation data, given the time that takes to obtain them. A Li-Ion battery is generally rated for a high number of cycles of operation at nominal values before is degraded (e.g. 2000 cycles), resulting in a slow procedure even with automatic battery cycling devices.

Chapter 5

Particle-Filternig-based Scheme for State-of-Charge Prognosis

The present chapter covers the implementation and validation of a SOC prognosis PF-based framework, and a proposal to include the battery internal temperature in it. It is organized as follows; First, it is introduced the proposed state-space model for the battery discharge, a methodology to obtain the model parameters, and the validation data. Then, the PF-based prognosis scheme is presented, including implementation issues and results. Finally, a manner to include the internal temperature of the battery in the scheme is proposed.

5.1 Model Proposal for a SOC Prognosis Scheme

This work proposes a SOC estimation and prognosis scheme, using an empirical state-space model inspired on electric equivalent circuits for the battery cell. Previous research efforts have also used a state-space representation to describe the SOC evolution in time. In [59] the proposed state-space model uses the traditional definition for the SOC (based on the battery capacity) and assumes a known look-up table to characterize the OCV. In contrast, an energy-based definition for the SOC is used in [60], although the parameterization that is proposed for the OCV curve is not appropriate to describe the real discharge evolution of a battery. Neither of them include the temperature of operation in the discharge model.

An electrochemical characterization is not considered, since they need to estimate numerous parameters (affecting the observability of the state vector), require extremely precise measurements for on-line implementation, and represent a high computational cost. In this regard, this work proposes an improved version of the energy-based approach presented in [60], emphasizing the efforts in a better state-space model to describe the battery discharge. In the proposed approach the SOC represents a percentage of the maximum amount of energy that can be stored in the battery.

This new model provides an adequate representation of the dynamics associated to the measured battery discharge voltage, in contrast to the previous representation that assumed a constant value for the open-circuit voltage for a wide range of SOC values. A discrete time characterization is assumed for the battery dynamics and the availability (real-time) of voltage and discharge current measurements. The structure of the proposed state-space model, presented in equations (5.1)-(5.3) offers a modification to the observation equation that incorporates most of the nonlinearities found in Li-Ion open-voltage discharge curves, while simultaneously enabling the implementation of reliable off-line estimation procedures for the estimation of all of its parameters. The concept of artificial evolution [35] has been applied to estimate the instantaneous absolute value of the battery internal impedance. This is implemented by extending the dimension of the state vector, and associating its first component x_1 with the value of this time-varying parameter.

State-of-Charge Dynamic Model

State transition equations:

$$x_1(k+1) = x_1(k) + \omega_1(k) \tag{5.1}$$
$$x_2(k+1) = x_2(k) - v(k) \cdot \mathrm{i}(k) \cdot \Delta t \cdot E_{crit}^{-1} + \omega_2(k) \tag{5.2}$$

Measurement equation:

$$v(k) = v_L + (v_0 - v_L) \cdot \mathrm{e}^{\gamma(x_2(k)-1)} + \alpha \cdot v_L \cdot (x_2(k) - 1) + ... \tag{5.3}$$
$$... + (1-\alpha) \cdot v_L \cdot \left(\mathrm{e}^{-\beta} - \mathrm{e}^{-\beta\sqrt{x_2(k)}}\right) - \mathrm{i}(k) \cdot x_1(k) + \eta(k)$$

In the proposed model the discharge current $\mathrm{i}(k)[A]$ and the sample time $\Delta t[sec]$ are input variables, and the battery voltage $v(k)[V]$ is the system output. The quantities v_0, v_L α, β, and γ are model parameters to be estimated offline. The states are defined as $x_1(k)$ (unknown model parameter) and $x_2(k)$ (SOC, remnant battery energy normalized by the parameter E_{crit}), E_{crit} is the expected total energy delivered by the ESD (that could be inferred from the nominal capacity or discharge curves included in datasheets). Process (ω_1 and ω_2) and measurement (η) noises are assumed Gaussian. It is important to mention that process noise ω_2 is correlated with η, the measurement noise, since the evolution in time of state x_2 depends on voltage measurements.

In the beginning of the filtering stage, most of the time there is no knowledge about the amount of energy stored in the battery. This implies that there is no information about the SOC and the initial condition of its associated state. To ensure its convergence to the real value during this stage, it is important to correct errors associated to incorrect initial conditions. This fact is a critical issue to guarantee an adequate initialization of the prognosis stage, which is based on the results of the filtering stage. This approach considers

an adaptive learning strategy [61] that increases the uncertainty associate with the state x_2 in (5.2) (through the manipulation of the variance of the process noise ω_2), based on the fact that changes on the internal battery impedance (and thus, the value associated to the state x_1) are negligible during a given discharge cycle [55]. Although this procedure helps to adjust the prior knowledge on the initial condition of the state vector, it may incorporate artificial sources of uncertainty within the Bayesian processor if kept invariant [61]. For this reason, and after a few battery voltage/current measurements are acquired, the variance is exponentially reduced, converging to a pre-defined lower bound (which is part of the PF implementation design parameters). This procedure, which can be considered as an outer feedback correction loop [61] in a failure prognostic routine, is critical to ensure a reasonable initial condition for the state vector.

5.1.1 Methodology for Measurement Equation Parameter Identification

In addition to the model itself, a methodology to obtain the parameters of the measurement equation (5.3) is proposed. It allows obtaining these parameters using only information from a single, prior, discharge test. This test (training data) is mainly used for offline estimation of parameters v_0, v_L α, β, and γ in (5.3), as well as the characterization of the prior distribution for $x_1(0)$. Equation (5.3) considers that the OCV curve has three different zones that require proper characterization, as shown in Figure 5.1. In the first zone, the OCV curve experiments an exponential decay as the SOC diminishes from a fully-charged condition to approximately 70%. In the second zone, the OCV basically presents an affine relationship with respect to the SOC (SOC between 70% and 25%). The third zone is characterized by an abrupt voltage drop with respect to small decrements in the SOC value. As the OCV curve is basically approximated as the sum of the voltage measured at battery terminals and a voltage drop caused by the battery internal impedance, the state-space model would become unobservable if all discharge tests were to consider constant currents. For this reason, we characterize the OCV curve using data from tests where at least two pulses are added to the battery discharge current. These pulses can be implemented at arbitrary time instants, as long as they take place inside Zone 2 (see Figure 5.1).

This experimental procedure can be easily implemented by approximating the E_{crit} parameter as the nominal battery energy. The purpose of these pulses is to estimate the absolute value of the internal impedance from the expression $|Z_p| = |\Delta V/\Delta I|$, assuming in $v_{oc}(k) = v(k) + \mathrm{i}(k) \cdot |Z_p|$, where $v(k)$ is the voltage measured at the terminals of the battery at time k, Z_p is the internal battery impedance and $v_{oc}(k)$ the open-circuit voltage at time k. Once $v_{oc}(k)$ and the internal impedance approximation for $|Z_p|$ are obtained using the aforementioned procedure, it is possible to estimate (off-line) the parameters that define the structure of measurement equation (5.3). To do this, the voltage discharge curve in Zone 2 is first modeled as $v_L + \alpha \cdot v_L \cdot (SOC - 1)$, where $\alpha \cdot v_L$ is the curve slope and v_L is the $y-$intercept of the curve when considering a reverse SOC axis (see Figure 5.1).

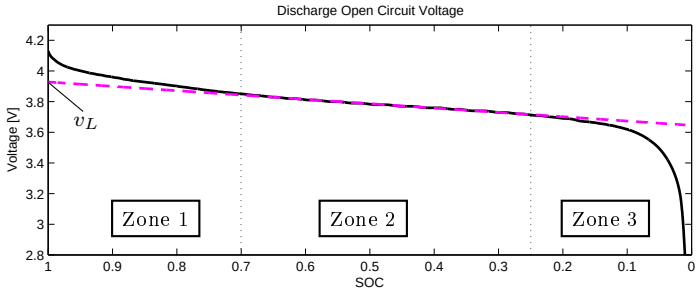

Figure 5.1: Li-Ion cell discharge open circuit voltage (dark black line) and linear zone projection (thin segmented magenta line) as a function of SOC (reversed x-axis).

Although this affine representation is sufficient to characterize Zone 2, a complete representation of the OCV discharge curve for the whole SOC range requires to incorporate additional terms to characterize Zones 1 and 3. Thus, for SOC values close to 1, the OCV curve includes the term $(v_0 - v_L) \cdot \mathrm{e}^{\gamma \cdot (SOC-1)}$, where v_0 is the OCV when the battery is fully charged (value that can be easily measured before performing the test) and the parameter γ may be obtained by minimizing the mean squared error (MSE) with respect to the measured OCV curve in Zone 2. Finally, to represent the abrupt voltage drop that occurs at low SOC values, it is necessary to add the term $(1-\alpha) \cdot v_L \cdot \left(\mathrm{e}^{-\beta} - \mathrm{e}^{-\beta\sqrt{x_2(k)}}\right)$, where β minimizes the mean squared error (MSE) in Zone 3 with respect to the voltage measured in the battery terminals during discharge.

5.1.2 Validation Data

Three different Li-Ion batteries were used to validate the efficacy of the model and the proposed off-line parameter estimation methodology. Training data were collected by implementing the discharge profile at nominal constant current that is illustrated in Figure 5.2. Cells used on these experiments were discharged until the voltage dropped to $0.5[V]$, although the manufacturer recommends to operate them with a safety lower voltage of $2.8[V]$. In real applications, either for safety reasons or constant-power load requirements, the high voltage drop that occurs at low SOC values may not be reached. However, for identical reasons, model errors for that specific operating zone may not be relevant.

Validation data set #1 (see Figure 5.3) consist of a Li-Ion 18650 cell (Battery #7; $3.7[V]$, $2.4[Ah]$) discharged with a profile that emulates the operation of a four-wheel ground robot [62], where the maximum and minimum current values were defined as $2.809[A]$ and $1.619[A]$, respectively. Validation data set #2 (see Figure 5.4) corresponds to a discharge test for a Li-Ion 18650 cell (Battery #8; $3.7[V]$, $3[Ah]$), where the battery current discharge profile is computed as a realization of a two-state Markov chain with transition probabilities $p_{11} = p_{21} = 0.55$, $p_{12} = p_{22} = 0.45$, and where the states are defined in terms of the value of the discharge current (state #1: $1[A]$, state #2: $3[A]$). Validation data set #3 (Figure 5.5) uses a Li-Ion/LiNiCoMn 26650 cell (Battery #9; $3.7[V]$, $4[Ah]$), which is discharged with a current usage profile that emulates and adapts the $FUDS$ test. This test is adapted with

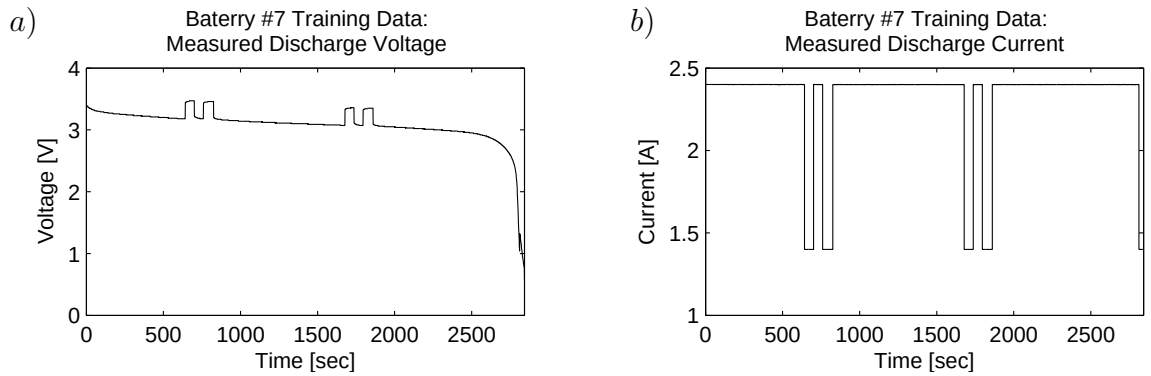

Figure 5.2: Model identification data for Battery #7: (a) measured voltage discharge and (b) measured current discharge data.

the same procedure as the explained until the fifth step in Section 3.1.1 (see Figure 3.6), but with a lower discharge current of 2.5$[A]$ and a maximum current value of 7$[A]$ for a 100% discharge power. As can be seen in Figure 5.5.b, the proposed discharge profile covers a wide range of current values. Table 5.1 shows the parameters obtained for each battery using the methodology proposed.

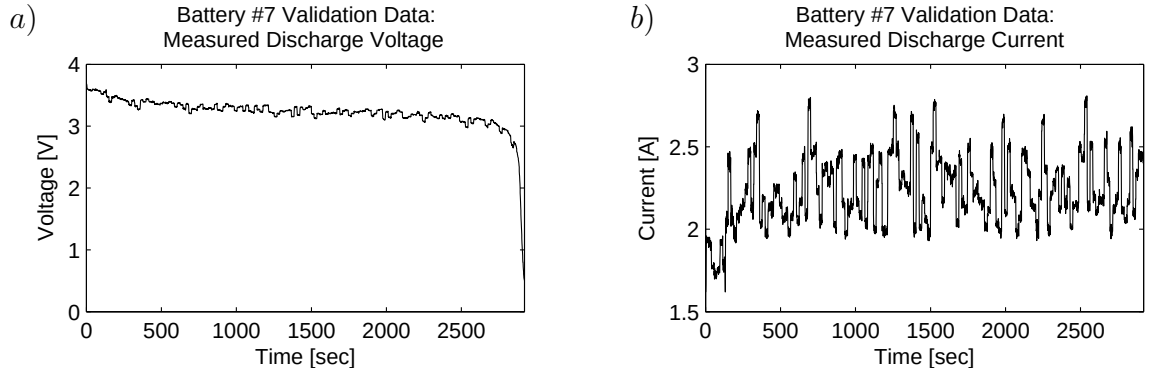

Figure 5.3: Validation data set for Battery #7: (a) measured voltage discharge and (b) measured current discharge

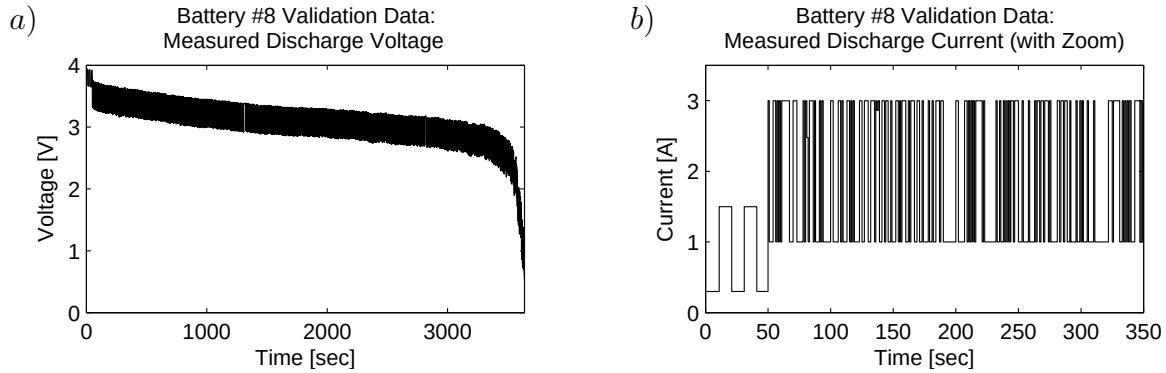

Figure 5.4: Validation data set for Battery #8: (a) measured voltage discharge and (b) measured current discharge.

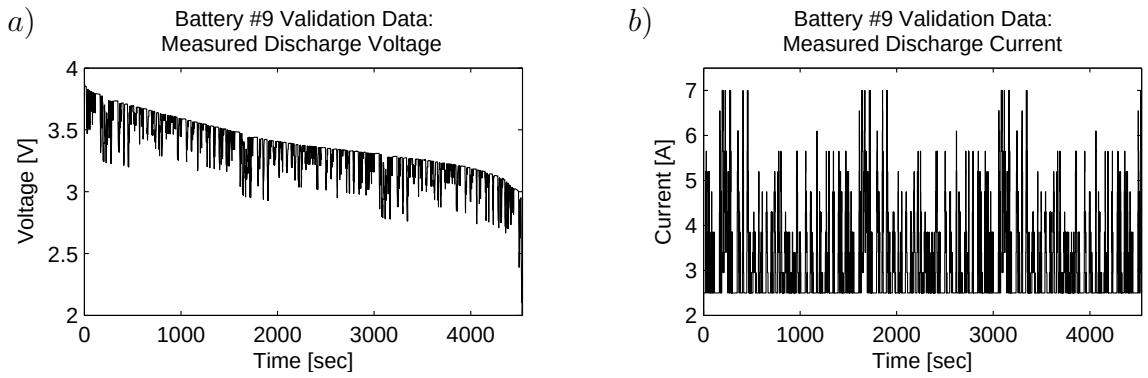

Figure 5.5: Validation data set for Battery #9: (a) measured voltage discharge and (b) measured current discharge

Table 5.1: Model Parameters for Batteries #1, #2 and #3.

Battery	α	β	γ	$\mathbf{v_0}$	$\mathbf{v_L}$	$\mathbf{E_{crit}}$	$\mathbf{\lvert Z_p \rvert}$
#1	0.08	16	19.65	4.12	3.987	20127	0.30
#2	0.15	12	6.61	4.00	3.813	19865	0.20
#3	0.15	17	10.50	4.14	3.997	46858	0.12

5.2 Issues Related to the Implementation of the SOC Prognosis Scheme

In practical applications the future discharge profile (i(k); $k > k_{predict}$) is unknown, and thus there is at least one additional source of uncertainty that needs to be characterized. To solve this problem, an statistical characterization of the usage profile introduced in [60] is implemented. With their approach, the future usage profile is modeled as the realization of a two-states Markov chain (MC). The states values and transition probabilities of the MC are obtained studying the current consumption during the filtering stage, using an adaptive scheme to give more importance to the last measurements. The generation of these future usage profiles is implemented without any other modification to the presented in [60]. Every realization of the MC implies a different future current consumption profile, and for each filtering result several different predictions can be made. To achieve the SOC prognosis, then for one realization of the filtering stage a given number of realizations of the MC are considered. The prognosis result can be obtained combining these predictions by the law of total probabilities.

As similar as in the case of the SOH prognosis scheme (see Section 4.2.1), it is important to determine the best algorithm parameters that should be used in SOC prognostic applications. More specifically, to focus on (i) the number of particles that need to be considered to represent the state PDF in each realization of the stochastic predictive model, (ii) the number of realizations of the filtering algorithm that are required to ensure standards in terms of accuracy of the predicted EOD PDF, and (iii) the number of realization of the Markov chain (MC) necessary for an adequate characterization of the different future discharge profiles at which the ESD could be operated, where each realization of the MC corresponds

to a possible future usage of the ESD through a sequence of the current states. A similar procedure as the discussed in Section 4.2.1, that compares the suboptimal solution with respect to an analytic solution for a simplified model was implemented in [60] (with a similar approach for the battery discharge model (5.1)-(5.3)). That determines that 25 realizations of the implemented MC are adequate, conditional to the fact that the implementation of the PF-based prognostic algorithm uses 40 particles and 25 realizations of the Bayesian filter to characterize the uncertainty associated to the state.

5.3 Validation of the SOC Prognosis Module

Validation of the proposed approach has been performed using the data from three different Lithium-Ion cells (as described in Section 5.1.2), and using performance measures (2.49) and (2.50), defining the End-of-Discharge as the End-of-Life ($EOD = EOL$) and a failure threshold $f_{th} = 0.05$ ($SOC = 5\%$). The ground truth EOD occurred at 2738[sec], 3381[sec] and 4283[sec] of operation for batteries #7, #8 and #9 respectively. Initial condition for the state x_2 is arbitrarily generated as a uniform random variable $[0.80, 0.90]$, even when it was known that in all experiments the batteries were always fully charged. The latter intended to demonstrate how well the estimation algorithm responds to erroneous initial conditions. Provided that PF-based EOD estimates are random variables, the validation analysis included several realization of the filter for each data set. Figures will only illustrate results for one particular realization, whereas Tables 5.2, 5.3 and 5.4 intend to aggregate information from all computed realizations.

Figure 5.6 and Figure 5.7 show the results of the prognostic algorithm using a (random) single realization of the PF-estimation algorithm and one of the 25 realizations of the Markov chain that characterizes the future battery use profile. EOD prognosis is computed at the 1800th [sec] of operation for Battery #7 and #8, and at the 2947^{th}[sec] for Battery #9. In these three cases, the proposed method and model structure allow to quickly overcome the problem of erroneous initial conditions for the state x_2, obtaining reliable estimates of the SOC in terms of the conditional expectation of the PF-based PDF estimate. Furthermore, the predicted output voltage for Battery #7 (see Figure 5.6.c) correctly includes a characterization of the voltage drop that occurs when the SOC reaches less than 10% (even considering that this event occurs at late stages within the prediction routine). However, Figure 5.7.c) shows an early voltage drop for the output voltage of the Battery #9 at a SOC of 6%, due to a higher uncertainty associated to the usage profile (with respect to Batteries #7 and #8). The resulting EOD PDF estimate allows building 95% confidence intervals for the discharge event; assuming that the statistical characterization of the system input (discharge profile) is invariant. Although this graphical information is useful to illustrate the system autonomy, it is incomplete because it is first necessary to evaluate the response of the filter to various realizations of the innovation process. Tables 5.2, 5.3 and 5.4 present the results obtained when running at least 5 different instances of the proposed approach, considering that each instance implies a single realization of the PF algorithm to estimate the state PDF at the 1800^{th}[sec] of operation in the case of Battery #7 and #8, or 2947^{th}[sec] of operation in the

case of Battery #9, and 25 realizations of the Markov chain that characterizes the future battery use profile. These results show that the proposed method can be used to statistically quantify the effect that random changes in the battery discharge current have on the ESD SOC.

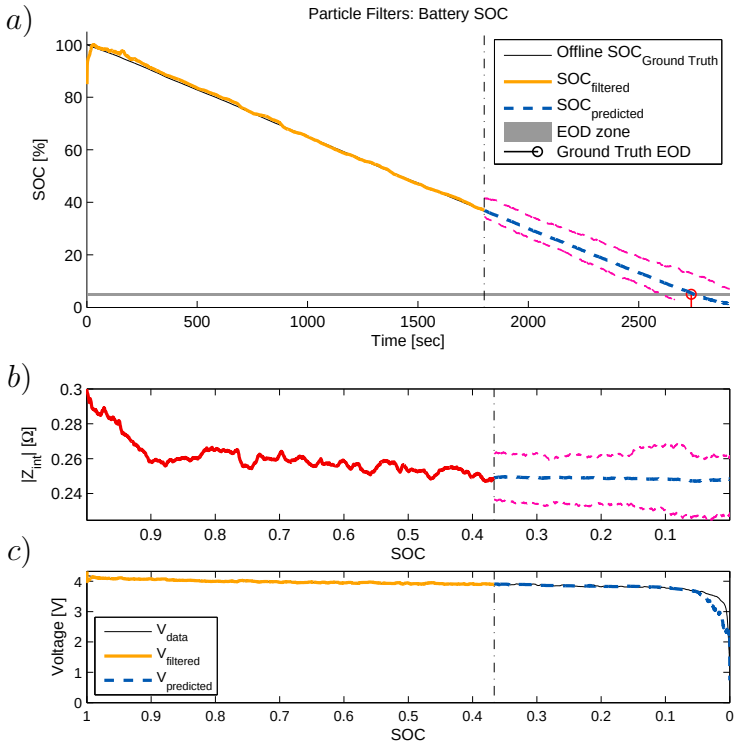

Figure 5.6: SOC prognosis for Battery #7 using the proposed PF-based framework. (a) Estimated SOC (bold orange line), predicted SOC (bold blue dashed line), and 95% confidence interval for SOC prediction (thin segmented magenta line), EOD threshold is defined as 5% SOC (red stem). (b) Evolution of the state x_1, as a function of SOC, during the estimation (solid red line), prediction (blue dashed line) stages and 95% confidence interval for x_1 prediction (thin segmented magenta line). (c) Measured voltage (thin black line), estimated voltage (orange line), and predicted voltage drop (dashed bold blue line), as a function of SOC.

EOD estimates presented in Table 5.2 show that the EOD expectation is, indeed, a random variable. Furthermore, it may happen that some realizations of this random variable underestimate (or overestimate) the ground truth EOD. Nevertheless, the obtained estimates (for both batteries) are sufficiently accurate. More importantly, they tend to underestimate the EOD; thus minimizing the probability of unexpected failure (conservative approach). In fact, the values obtained for the $JITP_{\gamma\%}$ in Table 5.2 are always smaller than the ground truth EOD, thus ensuring a safety utilization of the ESD. The maximum overestimation error in the conditional expectation is only of 23[*sec*], over a 938[*sec*] prediction window. The EOD conditional expectation estimates for Battery #8 and #9 are presented in Table 5.3 and 5.4 respectively, following a similar procedure as in the case of Battery #7. In those cases, all prognosis results provide EOD conditional expectations that underestimate the EOD ground truth. The proposed method obtained a maximum error of 116[*sec*] and 222[*sec*] for Battery #8 and #9; while the prediction horizon was 1581[*sec*] and 1336[*sec*], respectively. As the

characterization of the future usage profile for Battery #8 is made with realizations of a two state Markov chain, the prognosis stage leads to better results compared with Battery #9. This difference produces a higher underestimation of the EOD expectation for Battery #9. Underestimation of the EOD is not critical when compared to its overestimation, since the latter would lead to make wrong decisions in terms of systems autonomy. Figure 5.8 shows an illustration of the EOD PDF estimate, including the expectation and 95% confidence interval limits (ground truth EOD: 4283[*sec*]).

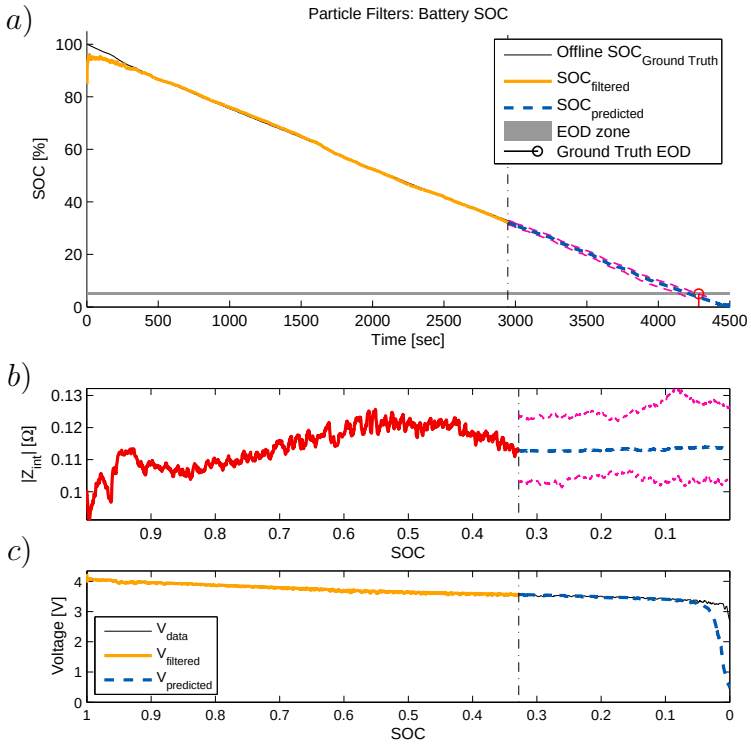

Figure 5.7: SOC prognosis for Battery #9 using the proposed PF-based framework. (a) Estimated SOC (bold orange line), predicted SOC (bold blue dashed line), and 95% confidence interval for SOC prediction (thin segmented magenta line), EOD threshold is defined as 5% SOC (red stem). (b) Evolution of the state x_1, as a function of SOC, during the estimation (solid red line), prediction (blue dashed line) stages and 95% confidence interval for x_1 prediction (thin segmented magenta line). (c) Measured voltage (thin black line), estimated voltage (orange line), and predicted voltage drop (dashed bold blue line), as a function of SOC.

Considering the length of the long-term prediction windows, the maximum error between the ground truth and the expected EOD correspond to only 2.45%, 7.3% and 16.6% for Battery #7, Battery #8, and Battery #9, respectively. Also, the corresponding maximum lengths for the obtained confidence intervals are 30.6%, 9.4%, and 11.8% of the prediction window. These results show that the proposed prognosis SOC framework presents a trade-off between the accuracy and precision of EOD estimates. In terms of Just in Time Point estimates, the maximum difference between the ground truth EOD and the JITP5% & JITP15% values are 184 and 142[*sec*] respectively (19.6% and 15.1% of the prediction window) for Battery #7. In the case of Battery #8, that difference is 195 and 160[*sec*], respectively (12.3% and 10.1% of the prediction window). For Battery #9, the difference is 309 and 280[*sec*],

respectively (23.1% and 20.9% of the prediction window). All these results provide reliable information for decision making process associated to the ESD autonomy.

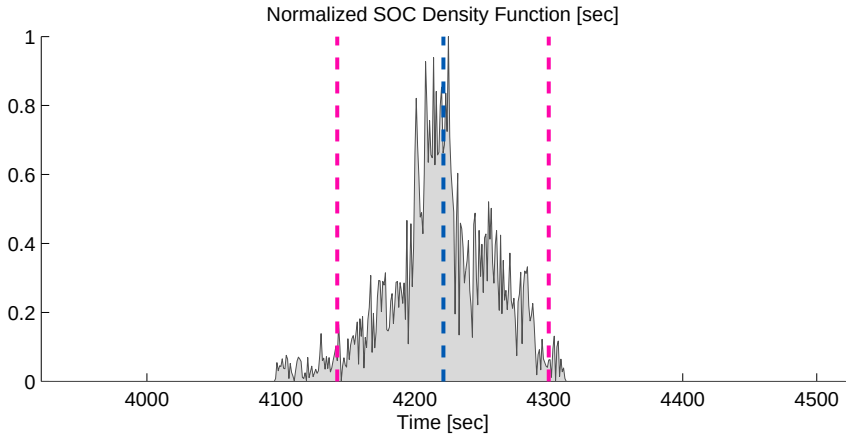

Figure 5.8: EOD PDF estimate (normalized) for Battery #9. Vertical dashed lines show the PDF expectation and the limits of the 95% confidence interval. Ground truth EOD is 4283[*sec*].

Table 5.2: Results for Different Realizations of the Proposed PF-Based SOC Prognosis Module (Battery #7). Ground Truth EOD: 2738 [sec].

Nº	**E{EÔD}**[*sec*]	**95% Confidence Interval [sec]**	**JIT$_{5\%}$ [sec]**	**JIT$_{15\%}$** [*sec*]
1	2643	[2552 ; 2741]	2572	2594
2	2751	[2612 ; 2892]	2632	2669
3	2634	[2600 ; 2669]	2600	2612
4	2670	[2533 ; 2820]	2554	2596
5	2761	[2653 ; 2876]	2675	2700

Table 5.3: Results for Different Realizations of the Proposed PF-Based SOC Prognosis Module (Battery #8). Ground Truth EOD: 3381 [sec].

Nº	**E{EÔD}**[*sec*]	**95% Confidence Interval [sec]**	**JIT$_{5\%}$ [sec]**	**JIT$_{15\%}$** [*sec*]
1	3317	[3244 ; 3390]	3237	3266
2	3324	[3249 ; 3398]	3240	3272
3	3265	[3215 ; 3314]	3174	3226
4	3287	[3215 ; 3359]	3203	3237
5	3303	[3255 ; 3350]	3246	3267

Table 5.4: Results for Different Realizations of the Proposed PF-Based SOC Prognosis Module (Battery #9). Ground Truth EOD: 4283 [sec].

Nº	**E{EÔD}**[*sec*]	**95% Confidence Interval [sec]**	**JIT$_{5\%}$ [sec]**	**JIT$_{15\%}$** [*sec*]
1	4118	[4050 ; 4187]	4025	4059
2	4115	[4044 ; 4186]	3997	4034
3	4073	[4010 ; 4136]	3974	4005
4	4061	[4013 ; 4109]	3981	4003
5	4101	[4023 ; 4180]	4002	4038

5.4 Proposal for Temperature Inclusion on the SOC Prognosis Scheme

Model parameters and validation data of the SOC PF-based prognosis scheme were obtained at an ambient temperature of 23[^oC]. The current profile described in the methodology for parameter identification (see Figure 5.2) has similar characteristics than the used to generate the data of delivered capacity in a cycle as a function of the temperature (see Figure 3.14). This implies that for each temperature of operation, a model parameter set v_0, v_L α, β, and γ can be calculated. Furthermore, E_{crit} can be established with the concept of "Usable Energy", similar to the "Usable Capacity" presented in Chapter 4, with the energy instead of the capacity. The initial condition of the state x_1 can be set using the results of approximated internal impedance at different temperatures presented in Section 3.2.2 (see Figure 3.17).

Figures 5.9.a and 5.9.b show the approximated OCV evolution of the discharges corresponding to Figure 3.14 as a function of the SOC and the time, respectively. The proposed model for the discharge evolution lies on the predominant linear relation between the OCV and the SOC. In this regard, the model cannot be applied for temperatures lower than 10[^oC]. Table 5.5 presents the results of the proposed methodology in Section 5.1.1 on the data presented in Section 3.2.1.

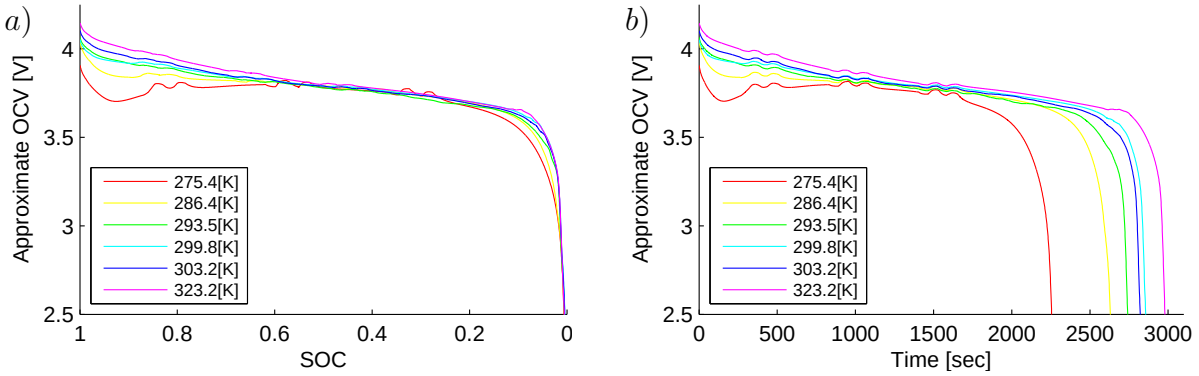

Figure 5.9: Temperature-dependentdt voltage discharge data with respect to (a) time, and (b) SOC.

Table 5.5: Model Parameters at Different Temperatures of Operation.

Temperature $[K]$	α	β	γ	$\mathbf{v_0}$	$\mathbf{v_L}$	$\mathbf{E_{crit}}$	$\mathbf{\lvert Z_p \rvert}$
286.37	0.0490	11.5	50.00	4.04	3.88	19042.87	0.24
293.48	0.0689	14.5	22.52	4.10	3.95	20272.61	0.21
299.76	0.0687	15.0	34.95	4.04	3.92	21055.36	0.23
303.15	0.0682	15.6	16.15	4.22	4.04	20859.13	0.22
323.22	0.0852	15.0	16.18	4.15	3.98	22311.44	0.22

Considering a similar procedure to be applied to batteries over $10[^{\circ}C]$, with improved operational conditions (adequate temperature chamber; better connections), a fuzzy model [63] could be implemented to include the temperature effect on the parameters of the model (5.1)-(5.3). Furthermore, a fuzzy approach should not only be suitable to include the internal temperature in the model, but also the C-rate. Both variables are two of the most important operational conditions to consider within a SOC estimation and prognosis scheme.

5.5 Final Remarks of This Section

This work proposes a new SOC state-space model to characterize discharge processes in Li-Ion batteries using a reduced number of parameters within the measurement equation. A methodology is also proposed to estimate those parameters using data from just one complete discharge test. The prognosis scheme was validated for Li-Ion cells operating at room temperature. Additional research activities are still required to generate an adequate temperature-dependent SOC model that could be used for prognosis purposes. In this regard, a way to incorporate the temperature in the state-space model is hereby suggested; but not validated. being crucial for this purpose to generate battery discharge data with different current profiles at multiple temperatures of operation.

Chapter 6

Conclusion

This work presents improved prognosis strategies for the SOH and SOC in Li-Ion batteries. Although both problems were covered separately, the efforts to achieve improvements to one of them can be used for the other one (study of the phenomenology of the batteries; laboratory experiments; modifications to the estimation algorithm). The principal objectives are to include the impact of the temperature on SOH/SOC PF-based estimation and prognosis schemes, in addition to improvements to the estimation stage. These were achieved from the results of a set of experimental tests with Li-Ion cells to understand the impact of the temperature on their performance, and the usage of existent public data bases.

The SOH prognosis problem is treated with a new empirical state-space model to describe the battery degradation evolution. An outer-feedback correction loop is implemented to allow the state x_1 to converge around its real value in presence of erroneous initial conditions (by varying the process noise ω_1). To work with outliers or lost data an hypothesis-test-based module is included in the estimation stage. When a new measurement is considered invalid, then the algorithm is able to generate predictions about the state vector, restarting the filtering stage when a new available measurement is valid. The proposed model includes an important factor of the batteries phenomenology: the temperature of operation. The concept of "Usable Capacity" make it possible to include the average temperature of operation during a cycle as an external input to the degradation model. As a consequence, the SOH estimation and prognosis are conducted at a reference temperature. This result is important because it allows to handle temperature-varying degradation data, and make long-term predictions at a nominal temperature. This scheme is validated using public available and laboratory-generated degradation data, but some extra test are required for a complete validation. As the generation of battery degradation data at different temperatures is a slow procedure (even more with the absence of an automatic cycling equipment and a temperature chamber), an artificially generated data set is introduced to test the performance of the scheme. This scheme allows to prognosticate the SOH of a battery at a reference temperature, generating a conditional PDF of x_1 for each future cycle. The latter allows to obtain indicators as confidence intervals, expectations or $JITP$ points.

A particle-filtering-based SOC/EOD prognostic approach has been proposed, tested, and validated. An empirical state-space model, inspired on the battery phenomenology, was also hereby introduced and validated. The model allows the implementation of Bayesian filtering methods that efficiently (and effectively) estimated SOC in real-time. Furthermore, the implementation of an outer correction loop during the filtering stage (to modify the variance of the process noise ω_2) provided quick adaptation for erroneous initial conditions. This reduced dramatically the associated impact on the EOD estimate bias. SOC/EOD prognosis is implemented using a PF-based method that considers a statistical characterization of future discharge profiles. Experimental results prove that the proposed framework allows to successfully prognosticate the discharge time in terms of conditional expectations, 95% confidence intervals, and $JITP_{\gamma}\%$ points. This offers conservative (but accurate) EOD estimates that help to minimize the probability of unexpected failure and ensuring a safe utilization of the ESD. Finally, a proposal to include the internal temperature of the battery in the discharge model was introduced.

Despite of the advances in both schemes, there is still work needed to be able to implement them in a real system like an electric vehicle or a micro-grid. With the inclusion of the temperature this thesis establishes a good basis to keep working with the objective of a fully functional SOH/SOC prognosis scheme under a stochastic approach.

Future work:

Further work is required for the SOH and SOC prognosis given the amount of operational conditions that determines the behavior and aging of batteries. The incorporation of variables as the Depth of Discharge (DOD) or the discharge rate (C-rate) are necessary for both SOH and SOC models. By this reason a set of experimental tests are needed to isolate the influence of each one, in addition to experiments where the DOD, C-rate and temperature are combined. The SOH model should also incorporate the time elapsed between each cycle as an extra input. Thinking in the implementation of both schemes in a BMS, their mutual dependence has to be considered. On the one hand the estimator of the SOC can be used to estimate the DOD, being an input for the SOH model. On the other hand, battery aging needs to be included in the SOC model (because affects the amount of energy that the battery can store), and SOH becomes and input.

From an experimental point of view, it is also interesting to study and evaluate these prognosis schemes in battery packs instead of cells. In some cases battery packs does not count with an array of sensors to monitor every individual cell, and a bounded number of sensors are used for the whole pack. Battery imbalance and temperature distribution inside the pack are factors that may result in cells aging differently, and would be worthy to include them in the schemes.

Algorithmic improvement could be achieved by studying variations to the classic particle filters, to the artificial evolution, or the parameter estimation. The SOH prognosis algorithm

could be improved including phenomenology of the battery, by generating a set of adequate degradation data in various operational conditions.

Bibliography

[1] B. Pattipati, C. Sankavaram, and K. Pattipati, "System identification and estimation framework for pivotal automotive battery management system characteristics," *Transactions on Systems, Man, AND CYBERNETICS - PART C: APPLICATIONS AND REVIEWS*, vol. 41, pp. 869–884, 2011.

[2] D. H. Jeon and S. M. Baek, "Thermal modeling of cylindrical lithium ion batttery during discharge cycle," *Energy Conversion and Management*, vol. 52, pp. 2973–2981, 2011.

[3] T. Mommaa, M. Matsunaga, D. Mukoyama, and T. Osaka, "AC impedance analysis of lithium ion battery under temperature control," *Journal of Power Sources*, vol. 216, pp. 304–307, 2012.

[4] D. Linden and T. Reddy, *Handbook of Batteries*, 3rd ed. McGraw-Hill, 2002.

[5] P. Arora and Z. Zhang, "Battery separators," *Chem. Rev.*, vol. 104, pp. 4419–4462, 2004.

[6] J. Moreira, C. Nascimento, and L. Rodrigues, "Health monitoring and remaining useful life estimation of lithium-ion aeronautical batteries," *IEEE*, 2012.

[7] M. Urbain, S. Raël, B. Davat, and P. Desprez, "Energetical modelling of lithium-ion battery discharge and relaxation," *Power Electronics Specialists Conference IEEE*, pp. 3628 – 3634, 2008.

[8] M. H. Miles, "Recent advances in lithium battery technology," *Gallium Arsenide Integrated Circuit (GaAs IC) Symposium, 2001. 23rd Annual Technical Digest IEEE*, pp. 219 – 222, 2001.

[9] F. Kalhammer, B. Kopf, D. Swan, V. Roan, and M. Walsh, "Status and prospects for zero emissions vehicle technology," State of California Air Resources Board Sacramento, California, Tech. Rep., April 2007.

[10] B. Scrosati and J. Garche, "Lithium batteries: Status, prospects and future," *Journal of Power Sources*, vol. 195, pp. 2419–2430, 2010.

[11] J. Voelcker, "Lithium batteries take to the road," *IEEE Spectrum*, 2007.

[12] J. Vetter, P. Novák, M. Wagner, K. M. C. Veit, J. Besenhard, M. Winter, M. Wohlfahrt-Meherns, C. Volger, and A. Hammouche., "Ageing mechanisms in lithium-ion batteries,"

Journal of Power Sources, vol. 147, pp. 269–281, 2005.

[13] A. Barré, B. Deguilhem, S. Grolleau, M. Gérard, F. Suard, and D. Riu, "A review on lithium-ion battery ageing mechanisms and estimatios for automotive applications," *Journal of Power Sources*, vol. 241, pp. 680–689, 2013.

[14] C. Zhou, K. Qian, M. Allan, and W. Zhou, "Modeling of the cost of EV battery wear due V2G application in power systems," *IEEE Transactions on Energy Conversion*, vol. 26, no. 4, December 2011.

[15] N. Williard, M. Osterman, and M. Pecht, "Comparative analysis of features for determining state of health in lithium-ion batteries," *Inernational Journal of Prognostics and Health Management, ISSN 2153-2648*, 2012.

[16] S. Zhang, "The effect of the charging protocol on the cycle life of a Li-ion battery," *Journal of Power Sources*, vol. 161, pp. 1385–1391, 2006.

[17] S. Drouilhet and B. Johnson, "A battery life prediction method for hybrid power applications," *Presented at the 35th AIAA Aerospace Sciences Meeting and Exhibit, Reno, Nevada*, January 1997.

[18] Y. Tan, J. Mao, and K. Tseng, "Modelling of battery temperature effect on electrical characteristics of Li-ion battery in hybrid electric vehicle," *IEEE PEDS*, December 2011.

[19] N. T. Magazine, "Why did nissan develop a battery?" http://www.nissan-global.com/EN/TECHNOLOGY/MAGAZINE/ev_battery.html, Published: Feb. 2012 Visited: Oct. 2013.

[20] L. Lam, "A practical circuit-based model for state of health estimation of Li-ion battery cells in electric vehicles," Master's thesis, University of Technology Delft, 2011, august.

[21] SANYO, *SANYO Lithium ion datasheet Cell Type UR18650F*, August 2004.

[22] S. Choi and H. Lim, "Factors that affect cycle-life and possible degradation mechanisms of a Li-ion cell based on $LiCoO_2$," *Journal of Power Sources*, vol. 111, pp. 130–136, 2002.

[23] P. Ramadass, B. Haran, R. White, and B. Popov, "Capacity fade of sony 18650 cells cycled at elevated temperatures part i. cycling performance," *Journal of Power Sources*, vol. 112, pp. 606–613, 2002.

[24] M. Takeno, M. Ichimura, K. Takano, J. Yamaki, and S. Okada, "Quick testing of batteries in lithium-ion battery packs with impedance-measuring technology," *Journal of Power Sources*, vol. 128, pp. 67–75, 2004.

[25] Z. Di, M. Yan, and B. Qing-Wen, "Estimation of lithium-ion battery state of charge," *30th Chinese Control Conference*, July 2011.

[26] M. Charkhgard and M. Farrokhi, "State-of-charge estimation for lithium-ion batteries

using neural networks and ekf," *IEEE Transactions on Industrial Electronics*, vol. 57, no. 12, pp. 4178–4187, December 2010.

[27] L. W. Yao and J. Aziz, "Modelling of lithium ion battery with nonlinear transfer resistance," *IEEE Applied Power Electronics Colloquium (IAPEC)*, pp. 104–109, 2011.

[28] B. Saha and K. Goebel, "Modeling li-ion battery capacity depletion in a particle filtering framework," *Annual Conference of the Prognostics and Health Management Society, San Diego, CA*, 2009.

[29] A. Ohnishi, N. Nagaoka, N. Mori, A. Ametani, and S. Umeda, "Automatic equivalent-circuit estimation system for lithium-ion battery," *43rd International Universities Power Engineering Conference, UPEC 2008.*, pp. 1–5, 2008.

[30] F. Barontia, G. Fantechi, L. Fanucci, E. Leonardi, R. Roncella, R. Saletti, and S. Saponara, "State-of-charge estimation enhancing of lithium batteries through a temperature-dependent cell model," *International Conference on Applied Electronics (AE)*, pp. 1–5, 2011.

[31] O. Erdinc, B. Vural, and M. Uzunoglu, "A dynamic lithium-ion battery model considering the effects of temperature and capacity fading." *International Conference onClean Electrical Power, Capri*, pp. 383–386, 9-11 June 2009.

[32] A. J. Salkind, C. Fennie, P. Singh, T. Atwater, and D. Reisner, "Determination of state-of-charge and state-of-health of batteries by fuzzy logic methodology," *Journal of Power Sources*, vol. 80, pp. 293–300, 1999.

[33] M. Dalal, J. Ma, and D. He, "Lithium-ion battery life prognostic health management system using particle filtering framework," *Proceedings of the Institution of Mechanical Engineers, Part O: Journal of Risk and Reliability*, vol. 225, pp. 81–90, 2011.

[34] C. Hu, B. D. Youn, and J. Chung, "A multiscale framework with extended kalman filter for lithium-ion battery SOC and capacity estimation," *Applied Energy*, vol. 92, pp. 694–704, April 2012.

[35] M. Orchard and G. Vachtsevanos, "A particle-filtering approach for on-line fault diagnosis and failure prognosis," *Transactions of the Institute of Measurement and Control 2009*, vol. 31, pp. 221–246, 2009.

[36] M. Cerda, "Estimación en línea del tiempo de descarga de baterías de ion-litio utilizando caracterización del perfil de utilización y métodos secuenciales de monte carlo," Master's thesis, Facultad de Ciencias Físicas y Matemáticas, Universidad de Chile, Santiago, Chile, 2012.

[37] M. Orchard, M. Tang, B. Saha, K. Goebel, and G. Vachtsevanos, "Risk-sensitive particle-filtering-based prognosis framework for estimation of remaining useful life in energy storage devices," *Studies in Informatics and Control*, vol. 19, pp. 209–218, September 2010.

[38] S. Santhanagopalan, Q. Zhang, K. Kumaresan, and R. E. White, "Parameter estimation and life modeling of lithium-ion cells," *Journal of The Electrochemical Society*, vol. 155, pp. A345–A353, 2008.

[39] B. Saha, K. Goebel, S. Poll, and J. Christophersen, "Prognostics methods for battery health monitoring using a bayesian framework," *IEEE Transactions on Instrumentation and Measurement*, vol. 58, pp. 291–296, 2009.

[40] P. Pascoe and A. Anbuky, "Standby vrla battery reserve life estimation," *Telecommunications Energy Conference INTELEC. 26th Annual International*, pp. 516–523, 2004.

[41] D. Andre, A. Nuhic, T. Soczka-Guth, and D. Sauer, "Comparative study of a structured neural network and an extended Kalman filter for state of health determination of lithium-ion batteries in hybrid electric vehicles," *Engineering Applications of Artificial Intelligence*, vol. 26, pp. 951–961, 2013.

[42] H. Wei, N. Williard, M. Osterman, and M. Pecht, "Remaining useful performance analysis of batteries," *IEEE Conference on Prognostics and Health Management (PHM)*, pp. 1–6, 2011.

[43] B. Olivares, "Sistema de pronónostico para el estado-de-salud de acumuladores de energía basado en filtro de partículas y caracterización estadística de fenómenos de regeneración," Master's thesis, Facultad de Ciencias Físicas y Matemáticas, Universidad de Chile, Santiago, Chile, 2012.

[44] E. Thomas, H. Case, D. Doughty, R. jungst, G. Nagasubramanian, and E. Roth, "Accelerated power degradation of Li-ion cells," *Journal of Power Sources*, vol. 124, pp. 254–260, 2003.

[45] L. Lam, P. Bauer, and E. Kelder, "A practical circuit-based model for Li-ion battery cells in electric vehicle applications," *Telecommunications Energy Conference (INTELEC), IEEE 33rd International*, October 2011.

[46] A. O. Dempster, "A generalization of Bayesian inference," *Journal of the Royal Statistical Society. Series B (Methodological)*, vol. 30, no. 2, pp. pp. 205–247, 1968.

[47] M. Mühlich, "Particle filters an overview," http://bi.snu.ac.kr/Courses/g-ai10f/Chapter%204%20PF%20Suppl%202%20-%20Muhelich%202003.pdf, Published: 2003 Visited: Oct. 2013.

[48] R. E. Kalman, "A new approach to linear filtering and prediction problems," *Journal of Basic Engineering*, vol. 82, pp. 35–45, 1960.

[49] J. V. Candy, *Bayesian Signal Processing: Classical, Modern, and Particle Filtering Methods*. A JOHN WILEY & SONS, INC., 2009.

[50] A. Doucet and A. Johansen, "A tutorial on particle filtering and smoothing: Fifteen years later," December 2008, v1.1.

[51] C. Musso, N. Oudjane, and F. L. Grand, *Sequential Monte Carlo Methods in Practice*. Springer, 2001, ch. Improving Regularised Particle Filters, pp. 247–271.

[52] A. Doucet, S. Godsill, and C. Andrieu, "On sequential monte carlo sampling methods for bayesian filtering," *Statistics and Computing*, vol. 10, pp. 197–208, 2000.

[53] S. Engel, B. Gilmartin, K. Bongort, and A. Hess, "Prognostics, the real issues involved with predicting life remaining," *AIEEE erospace Conference Proceedings*, vol. 6, pp. 457 – 469, 2000.

[54] United States Advanced Battery Consortium, *Electric Vehicle Battery Test Procedures*, revision 2 ed., January 1996.

[55] M. Chen and G. Rincon-Mora, "Accurate electrical battery model capable of predicting runtime and I-V performance," *IEEE Transactions on Energy Conversion*, vol. 21, pp. 504–511, 2006.

[56] B. Saha and K. Goebel, "Battery data set," http://ti.arc.nasa.gov/project/prognostic-data-repository, Visited: Oct.2007, nASA Ames Prognostics Data Repository, NASA Ames, Moffett Field, CA.

[57] B. Olivares, M. Cerda, M. Orchard, and J. Silva, "Particle-filtering-based prognosis framework for energy storage devices with a statistical characterization of state-of-health regeneration phenomena," *IEEE Transactions on Instrumentation and Measurement*, vol. 62, pp. 364–376, February 2013.

[58] D. Acuña, M. Orchard, J. Silva, and A. Pérez, "Multiple-imputation particle-filtering scheme for uncertainty characterization in battery state-of-charge estimation problems with missing measurement data," *Annual Conference of the Prognostics and Health Management*, 2014.

[59] W. He, N. Williard, C. Chen, and M. Pecht, "State of charge estimation for electric vehicle batteries using unscented kalman filtering," *Microelectronics Reliability*, vol. 53, no. 6, pp. 840–847, June 2013.

[60] M. Orchard, M. Cerda, B. Olivares, and J. Silva, "Sequential monte carlo methods for discharte time prognosis in lithium-Ion batteries," *International Journal of Prognostics and Health Management*, vol. 3, no. 10, pp. 1–12, 2012.

[61] M. Orchard, F. Tobar, and G. Vachtsevanos, "Outer feedback correction loops in particle filtering-based prognostic algorithms: Statistical performance comparison," *Studies in Informatics and Control*, vol. 18, pp. 295–304, December 2009.

[62] M. Orchard, P. Hevia-Koch, B. Zhang, and L. Tang, "Risk measures for particle-filtering-based state-of-charge prognosis in lithium-ion batteries," *IEEE Transactions on Industrial Electronics*, vol. 60, no. 11, pp. 5260–5269, November 2013.

[63] T. Takagi and M. Sugeno, "Fuzzy identification of systems and its applications to modeling and control," *IEEE Transactions on Systems, Man and Cybernetics*, vol. SMC-15,

no. 1, pp. 116–132, January/February 1985.